Topological Semimetal Driven by Strong Correlations and Crystalline Symmetry

Lei Chen[1], Chandan Setty[1], Haoyu Hu[1], Maia G. Vergniory[2,3], Sarah E. Grefe[4], Lukas Fischer[5], Xinlin Yan[5], Gaku Eguchi[5], Andrey Prokofiev[5], Silke Paschen[5,1,*], Jennifer Cano[6,7,*], and Qimiao Si[1,*]

[1]Department of Physics and Astronomy, Rice Center for Quantum Materials, Rice University, Houston, Texas 77005, USA

[2]Max Planck Institute for Chemical Physics of Solids, 01309 Dresden, Germany

[3]Donostia International Physics Center, P. Manuel de Lardizabal 4, 20018 Donostia-San Sebastian, Spain

[4]Theoretical Division, Los Alamos National Laboratory, Los Alamos, New Mexico 87545, USA

[5]Institute of Solid State Physics, Vienna University of Technology, Wiedner Hauptstr. 8-10, 1040 Vienna, Austria

[6]Department of Physics and Astronomy, Stony Brook University, Stony Brook, NY 11794, USA

[7]Center for Computational Quantum Physics, Flatiron Institute, New York, NY 10010, USA

arXiv:2107.10837v5 [cond-mat.str-el] 20 Jul 2022

Electron correlations amplify quantum fluctuations and, as such, they have been recognized as the origin of a rich landscape of quantum phases. Whether and how they lead to gapless topological states is an outstanding question, and a framework that allows for determining novel phases and identifying new materials is in pressing need. Here we advance a general approach, in which strong correlations[1,2] cooperate with crystalline symmetry[3,4] to drive gapless topological states. We test this materials design principle by exploring Kondo lattice models and materials whose space group symmetries may promote different kinds of electronic degeneracies, with a particular focus on square-net systems. Weyl-Kondo nodal-line semimetals – with nodes pinned to the Fermi energy – are identified. We describe how this approach can be applied to discover strongly correlated topological semimetals, identify three heavy fermion compounds as new candidates, provide first direct experimental evidence for our prediction in $Ce_2Au_3In_5$, and discuss how our approach may lead to many more. Our findings illustrate the potential of the proposed materials design principle to guide the search for new topological metals in a broad range of strongly correlated systems.

E-mails: qmsi@rice.edu; jennifer.cano@stonybrook.edu; paschen@ifp.tuwien.ac.at

Electron correlations and topology are well established as engines for surprising and potentially functional properties. Strong correlations promote quantum fluctuations, which engender abundant phases of matter and various quantum phase transitions[1,2]. Meanwhile, extensive developments have taken place in noninteracting electron systems, especially those with sizable spin-orbit couplings (SOC). In particular, the role of space group symmetry in determining and classifying symmetry-protected topological phases has been highlighted[4–8]. In the "hydrogen atom" version of topological semimetals in two and three dimensions (2D and 3D), space-group symmetry enforces Dirac nodes in the honeycomb lattice – as realized in graphene[9] – and diamond lattice[10], respectively. They set the stage for a systematic search of weakly correlated topological materials in terms of the constraints of space group symmetries on noninteracting bandstructures for a variety of crystal structures, which has led to a large topological materials database[11,12].

We can expect that the intersection of these two fields will be especially fertile in breeding novel quantum phases, but it remains a largely open terrain[13–15] especially for the case with gapless bulk excitations[2,16]. The fractional quantum Hall effect amply demonstrates the capability of strong correlations to drive gapped topological states. By contrast, correlated gapless electronic topology has been much less explored. The usual approach starts from noninteracting symmetry-protected topological states. It considers the interactions as a perturbation or as producing a symmetry-breaking ordered state – such as a magnetic order – that in turn modifies the weakly-correlated topology[3]. In the opposite limit, where the electrons' correlations dominate over their kinetic energy, there has been a considerable lack of strongly correlated gapless topological materials. It is pressing to realize such materials, which are important in their own right and may also serve as anchoring points to explore the overall landscape of strongly correlated gapless topology. Recently, a non-perturbative study has led to a Weyl-Kondo semimetal phase[17–19] in a toy model associated with the diamond lattice. Concurrently, such a phase was advanced experimentally in a cubic heavy fermion compound $Ce_3Bi_4Pd_3$ based on measurements of the specific heat and a spontaneous Hall effect[20–22]. The interplay between significant electron correlations and lattice geometry is also being explored experimentally in other materials such as the kagome metals[23–25].

These developments motivate the search for a general non-perturbative framework to treat the interplay of correlation and topology and design both phases and materials of correlated gapless electronic topology. Our hypothesis is that strong correlations cooperate with crystalline symmetry to produce such states. Specifically, as Fig. 1(a) illustrates, strong correlations give rise to emergent excitations *at low energies.* The space group symmetry constrains these excitations, leading to

emergent topological phases while enforcing their gapless nature. If validated, the proposition provides a materials design principle for correlated gapless electronic topology. Still, the proposed cooperation is counter-intuitive, because strong correlations tend to cause localization and gap out electronic excitations[26,27].

To test the proposed materials design principle, it is important to go beyond toy models and explore correlated systems with general space group symmetries that may promote different types of nodal electronic states. We illustrate our approach by narrowing down the choice of strong-coupling models for our study here as follows. We focus on space group symmetries where electronic degeneracies may develop at partial fillings, regardless of orbital content. These often happen in nonsymmorphic space groups. We examine the case where interactions do not break crystalline or time-reversal symmetries, as a point of principle. Finally, to be definite, we formulate our materials design in the context of Kondo lattice systems, as realized via the limit of strong Coulomb repulsion in periodic Anderson models. The Kondo effect leads to a ground state in which the local moments and conduction electrons entangle and form a spin singlet, which supports composite fermions in the excitation spectrum at low energies – within the Kondo energy scale of the Fermi energy[28–30]. Generalizations to other correlated systems will be discussed.

We thus consider a Kondo lattice system that contains mirror symmetry, which is known to favor Weyl nodal lines in noninteracting systems[31–34]. Our focus is on the nonsymmorphic and noncentrosymmetric square-net systems, which host both mirror and screw nonsymmorphic symmetries [Fig. 1(b)(c)]. Especially, space group (SG) 129 has been a fertile setting for electronic degeneracies of noninteracting systems[35–40] and is particularly advantageous in that the degeneracies are orbital-independent[5]. Allowing for inversion-symmetry breaking, we demonstrate the cooperation of strong correlations with space group symmetry in producing a novel phase – a Weyl-Kondo nodal-line semimetal. Our analysis of correlation-driven topological semimetal phases gives rise to a general procedure to design new materials that realize such phases. We illustrate this materials design principle by identifying several new candidate Ce-based correlated-topological semimetals, and indicate how it can be used to identify many new materials.

The periodic Anderson model (PAM) is specified by the following Hamiltonian:

$$\mathcal{H} = \mathcal{H}_d + \mathcal{H}_{cd} + \mathcal{H}_c \,. \tag{1}$$

The spin-$1/2$ d- and c-fermion operators describe the physical localized f electrons and the light spd conduction electrons that form the noninteracting bands, respectively. Further details of the

model and solution method are described in the Methods.

The 3D crystalline structure of SG 129 ($P4/nmm$) and its inversion-breaking counterpart, SG 31, are constructed by stacking 2D layers in the z-direction. To set the stage for analyzing the interplay between space group symmetry and correlation effects, we start from this 2D system corresponding to the layer group $p4/nmm$. The Hamiltonian of the conduction electrons, $\mathcal{H}_c$, is described in a matrix form: $\mathcal{H}_c = \sum_{\mathbf{k}} \Psi^\dagger_{\mathbf{k}} H_c(\mathbf{k}) \Psi_{\mathbf{k}}$, where $\Psi^T_{\mathbf{k}} = (c_{\mathbf{k}\uparrow A}, c_{\mathbf{k}\downarrow A}, c_{\mathbf{k}\uparrow B}, c_{\mathbf{k}\downarrow B})$, with A and B being the two sublattices, $\mathbf{k}$ the wavevector, and $\sigma =\uparrow,\downarrow$ marking the spin quantum numbers. As described in the Methods (and illustrated in Fig. S3), it contains tight-binding hopping terms between the nearest (t_1) and next-nearest (t_2) neighbors, an SOC (t^{SO}) term, and an inversion-symmetry-breaking (Δ) term. In the absence of the Kondo effect, all the electrons prefer to occupy the low-lying d-states to half filling, making the d-component to be a Mott insulator. Concomitantly, the conduction c-electron bands are completely empty, *i.e.* they lie above the Fermi energy. Figure 2(a) shows the bandstructure for the case of the inversion-symmetry-breaking potential $\Delta = 0$, *i.e.* in the presence of the full $p4/nmm$ symmetry. The mirror and screw nonsymmorphic symmetries enforce additional crossings at high symmetry points X, Y and M (see Methods)[35]. Since these Dirac points occur far above the Fermi energy, they leave the ground state topologically trivial. We note that the separated d-electrons are deep levels far away (below) the Fermi energy; they are half-filled and form a Mott insulator due to the large onsite Coulomb repulsion. Figure S1(a) shows the dispersion of the Kondo-driven, Fermi-energy bound, composite fermions for $\Delta = 0$. Because the composite fermion bands are subjected to the nonsymmorphic symmetry constraint, they feature Dirac nodes at X, Y and M.

We are now in position to present our main results on the 3D SGs 129 and 31. For SG 129, the mirror and screw symmetries have the same effect as in the 2D case. This implies that Kondo-driven, dispersive, Dirac nodes robustly develop along the XR, MA and YS lines in the composite-fermion spectrum within the Kondo energy of the Fermi energy. Their dispersive nature implies that a Dirac nodal point can develop at the Fermi energy. We illustrate this point through a concrete calculation [Supplementary Information (SI), Figs. S2(a)(b)]. We note that, in the presence of a magnetic field (or ferromagnetic order), Kondo-driven Weyl nodes develop [SI, Figs. S2(c)(d)].

The case of SG 31 is more involved. To be definite, we consider $\mathcal{AA}$ stacking of square-net layers as illustrated in Fig. 1(d), with the two stacking layers respectively hosting s and p orbitals[32,33]. The corresponding periodic Anderson model is given in the Methods. In the presence of the Kondo effect, our results are shown in Fig. 3(a). Nodes develop in the dispersion of the

Kondo-driven composite fermions, which are more clearly seen in Fig. 3(b) as we zoom in to the immediate vicinity of the Fermi energy. In our model, the Kondo-driven nodes are precisely at E_F. These electronic degeneracies appear in the form of Weyl-nodal lines in the $k_z = 0$ plane, as shown in Fig. 3(c). All these reflect the mirror nonsymmorphic $\{M_z|\frac{1}{2}\frac{1}{2}0\}$ symmetry. Because they are associated with the highly renormalized composite fermions, the Weyl nodal-line excitations have strongly reduced velocities. We stress that the nodal lines are robust against the SOC.

The realization of the Weyl-Kondo nodal-line semimetal is particularly important, as it suggests the emergence of drumhead surface states. We have computed the excitation spectrum on the (001) face in a slab with 40 unit cells. As indicated in Fig. 3(d), we find Kondo-driven drumhead surface states that are bounded by the projections of the Weyl rings. Importantly, the dispersion of the drumhead states also captures the Kondo energy scale and, hence, is strongly correlation-renormalized.

We now turn to the experimental signatures of the Kondo-driven nodal-line Weyl semimetals. The first category of the signatures bear similarities with those of the Weyl-Kondo semimetals[17–22]. For example, because the velocity v^* is highly reduced from the typical bare conduction-electron value v, the specific heat is expected to have a quadratic temperature dependence with a large enhancement factor (see the SI):

$$c_v = \Gamma\, T^2\,. \tag{2}$$

Here, the prefactor is $\Gamma = \frac{K}{2\pi}\frac{9\zeta(3)}{2}\left(\frac{k_B}{\hbar v^*}\right)^2 k_B$, where K is the length of the nodal line and the zeta function $\zeta(3) \approx 1.202$. It is enhanced from the typical noninteracting value by $(v/v^*)^2$, which is of the order $(W/k_B T_K)^2$, where W is the bare conduction-electron bandwidth. This enhancement factor is huge–about $10^4 - 10^6$ for moderately to strongly renormalized heavy-fermion semimetals. As another example, the enhanced Berry curvature near the Fermi energy can be probed through the spontaneous Hall effect[21].

The second category of experimental signatures are distinct for the Kondo-driven nodal-line phase. As one example, the nodal lines lead to a non-trivial Berry phase of any closed loop perpendicular to the mirror plane. The resulting characteristic signatures in quantum oscillations for such a strongly correlated setting are considerably more challenging to probe than their weakly correlated counterparts[41–43]. However, in materials with moderate mass enhancement (as we will identify below), these experiments are expected to be feasible. As another example, the drumhead surface states will lead to distinct spectroscopic signatures. They can, as in weakly correlated systems[44], in principle be probed by quasiparticle-interference measurements via scanning tunnel-

ing microscopy (STM); here, the quasiparticle-interference pattern develops structure at wavevectors whose magnitude is bounded from above by the location of the nodal lines in the bulk, as well as at energies that are bounded above by the bandwidth of the drumhead states[45]. Finally, developments of recent years[46] make angle-resolved photoemission spectroscopy (ARPES) as a promising probe of the dispersive bulk and surface f-electron states we have discussed.

We turn next to demonstrating how our approach guides the search for new correlation-driven topological materials. Because the composite fermions must be located near the Fermi energy, we can expect the Kondo-driven semimetal phases to host topological nodal excitations near the Fermi energy for generic fillings. Consequently, the cooperation of symmetry and Kondo correlation is adequate to realize candidate Kondo materials; this general procedure is outlined in Fig. 1(a). In passing, we note on one general point. Designing strongly correlated topological materials is inherently difficult; in the presence of strong correlations, *ab initio* calculations of electronic states represent a challenge. Here, we bypass this difficulty by using symmetry. Our results on the model Kondo lattice Hamiltonians imply that space group symmetry and Kondo correlation cooperate in driving correlated topological semimetals. Hence, we can design new materials for correlation-driven topological semimetals based purely on crystalline symmetry and strong correlations, without resorting to *ab initio* results for the correlated electronic structure.

We first consider SG 129, and focus on the case of the Ce ions on site 2c. The procedure is outlined in Fig. 4(a) and further described in the SI. It leads to two new materials, $CePt_2Si_2$ and $CeRh_2Ga_2$, which we propose to realize the Kondo-driven semimetal phase. Both remain paramagnetic down to the lowest temperature of somewhat below 2 K[47,48] that has been experimentally measured, and both have strong correlations as inferred from their moderately enhanced specific heat (see Supplementary Information). Moreover, both show semimetalic behavior. Below their respective Kondo temperatures, their resistivity as a function of temperature [Fig. S5(a)(b)] behaves similarly as the well-established heavy-fermion semimetals $Ce_3Bi_4Pd_3$ and CeNiSn[20,49], respectively [Fig. S5(c)(d)]. For $CePt_2Si_2$, the spd electronic structure, determined by f-core DFT calculations (see Methods), are displayed in Fig. 2(c). As can be seen, the symmetry of SG 129 dictates the existence of Dirac nodes at the X, M, R and A points, which are located away from the Fermi energy. The results for $CeRh_2Ga_2$ are similar (see the SI). The DFT-calculated electronic structure is expected to apply well above the Kondo temperature. Below their respective Kondo temperatures, the approach we have advanced here suggests that they will realize Kondo-driven topological semimetals. The precise nature of the renormalized band structure requires the con-

struction of tight-binding representations of the DFT-derived band structure as well as *ab initio* input of the Kondo couplings. We outline how this construction can be done in the SI, and reserve correlated *ab initio* studies for a future work. Still, our solution of the model Kondo lattice Hamiltonian with SG 129 and the resulting conclusion about the cooperation between the symmetry and Kondo correlation imply that both materials qualify as candidates for the correlation-driven topological semimetals advanced here.

Studies of these materials set the stage to search for additional strongly correlated semimetals. In the case of a nonzero inversion-symmetry-breaking term Δ, corresponding to SG 31, a similar search procedure for the Ce-based case is outlined in Fig. 4(b) and in the SI. It leads to the identification of a new material, $Ce_2Au_3In_5$, as a candidate heavy-fermion material that is known not to order down to the lowest measured temperature (2 K)[50]. Its inversion-symmetry breaking is illustrated in Fig. 4(e). We propose it as a candidate material to realize the Weyl-Kondo nodal-line semimetal advanced here. Thus, considerations of these two specific space groups lead to the identification of three new candidate Kondo-driven topological semimetals [Fig. 4(c)]. This result already considerably expands the material base for such strongly correlated topological semimetals beyond the known case of $Ce_3Bi_4Pd_3$[20–22].

To demonstrate the predictive power of our materials design principle, we have synthesized single-crystalline $Ce_2Au_3In_5$ and its La-counterpart, $La_2Au_3In_5$. The electronic specific heat of $Ce_2Au_3In_5$ is shown in Fig. 4(d) (see the SI for how the phonon contribution is determined). The low-temperature upturn indicates the influence of a (presumably magnetic) phase transition below the lowest measured temperature (2 K). In the paramagnetic regime free of this influence, a ΓT^2 form is observed. Fitting Γ in terms of Eqs. (2,S15) yields a nodal velocity $v^* = 2994$ m/s. This represents a close-to 3-orders of magnitude renormalization from the typical velocity of noninteracting electrons, which is consistent with the association with Kondo-driven composite fermions.

Our approach for materials design can be readily generalized. For example, our procedure applies to other Wyckoff positions (e.g., Ce ions at positions 2a or 2b instead of 2c), other lanthanide elements (Pr, Sm, Eu, Yb, in addition to Ce) and actinide elements (e.g., U) and, finally, a large number of other space group symmetries (in particular, those among the 155 nonsymmorphic space groups). These factors make it likely that hundreds of candidate materials can be realized for strongly correlated topological semimetals phases.

We now underscore some general lessons drawn from our results. Our models have an even number of electrons per unit cell. The typical localizing tendency of strong correlations could have

turned the systems into Kondo insulators[15,51,52]. Instead, the strong correlations cooperate with the space group symmetries [Fig. 1(a)]: the Kondo effect generates composite fermions; the space group symmetry constraints on the composite fermions prevent the Kondo gap from developing and lead instead to the Weyl nodal excitations.

Going beyond Kondo systems, emergent low-energy excitations can already develop for intermediate correlations, when the correlation strength is comparable to the noninteracting bandwidth. Here too, they will be subjected to space group symmetry constraints. To illustrate the point, consider a multi-orbital Hubbard model containing both Hubbard and Hund's interactions and with the orbitals having unequal kinetic energies[53,54]. When a correlated metal develops near an orbital-selective Mott phase, the emergent low-energy excitations take the form of a narrow band that is bound to the immediate vicinity of the Fermi energy, as indeed seen experimentally[55]. For such models in suitable crystalline settings, the space group symmetries are expected to constrain the low-energy excitations and produce gapless topological phases. Thus, our work motivates parallel (and systematic) studies for correlated gapless electronic topology in such multi-orbital models and the associated transition-metal compounds. We can expect our approach to provide a means for identifying hitherto-unknown phases and materials of correlated electronic topology in a variety of settings across a wide correlation spectrum. Finally, correlation physics that involves nontrivial electronic topology is a general problem that pertains to a growing list of materials. As recent studies[56] in the moiré bands of twisted bilayer graphene illustrate, the kind of topological heavy fermions we advance here may well serve as a platform to elucidate the enigmatic physics of these emerging materials.

In conclusion, we have advanced a materials design principle for strong correlations to cooperate with space group symmetry and drive correlated topological solids. Strong correlations lead to low-energy emergent excitations, which are subject to the constraints of the space group symmetry for topological phases. We have tested this approach in Kondo lattice models whose space group symmetries may promote different kinds of electronic degeneracies. In nonsymmorphic and noncentrosymmetric square-net systems, we have theoretically validated the approach by demonstrating novel Weyl-Kondo nodal-line semimetals in both two and three dimensions. The approach has allowed us to propose a general procedure to identify new materials for correlation-driven topological semimetals, to apply it and identify a number of such materials in several representative space groups, and to suggest that many others can be designed in this way. We have synthesized single-crystalline $Ce_2Au_3In_5$ and provided new experimental results to support the theoretical pre-

diction. Our findings illustrate the potential of the proposed materials design principle to guide the search for new correlated topological metals in a broad range of strongly correlated quantum materials.

---

1. Keimer, B. & Moore, J. E. The physics of quantum materials. *Nat. Phys.* **13**, 1045 (2017).
2. Paschen, S. & Si, Q. Quantum phases driven by strong correlations. *Nat. Rev. Phys.* **3**, 9 (2021).
3. Armitage, N. P., Mele, E. J. & Vishwanath, A. Weyl and Dirac semimetals in three-dimensional solids. *Rev. Mod. Phys.* **90**, 015001 (2018).
4. Cano, J. & Bradlyn, B. Band representations and topological quantum chemistry. *Annu. Rev. Condens. Matter Phys.* **12**, 225–246 (2021).
5. Bradlyn, B., Elcoro, L., Cano, J., Vergniory, M. G., Wang, Z., Felser, C., Aroyo, M. I. & Bernevig, B. A. Topological quantum chemistry. *Nature* **547**, 298–305 (2017).
6. Cano, J., Bradlyn, B., Wang, Z., Elcoro, L., Vergniory, M. G., Felser, C., Aroyo, M. I. & Bernevig, B. A. Building blocks of topological quantum chemistry: Elementary band representations. *Phys. Rev. B* **97**, 035139 (2018).
7. Po, H. C., Vishwanath, A. & Watanabe, H. Symmetry-based indicators of band topology in the 230 space groups. *Nat. Commun.* **8**, 50 (2017).
8. Watanabe, H., Po, H. C., Zaletel, M. P. & Vishwanath, A. Filling-enforced gaplessness in band structures of the 230 space groups. *Phys. Rev. Lett.* **117**, 096404 (2016).
9. Castro Neto, A. H., Guinea, F., Peres, N. M. R., Novoselov, K. S. & Geim, A. K. The electronic properties of graphene. *Rev. Mod. Phys.* **81**, 109–162 (2009).
10. Fu, L., Kane, C. L. & Mele, E. J. Topological insulators in three dimensions. *Phys. Rev. Lett.* **98**, 106803 (2007).
11. Vergniory, M. G., Elcoro, L., Felser, C., Regnault, N., Bernevig, B. A. & Wang, Z. A complete catalogue of high-quality topological materials. *Nature* **566**, 480–485 (2019).
12. Zhang, T., Jiang, Y., Song, Z., Huang, H., He, Y., Fang, Z., Weng, H. & Fang, C. Catalogue of topological electronic materials. *Nature* **566**, 475–479 (2019).
13. Maciejko, J. & Fiete, G. A. Fractionalized topological insulators. *Nat. Phys.* **11**, 385 (2015).
14. Rachel, S. & Le Hur, K. Topological insulators and Mott physics from the Hubbard interaction. *Phys. Rev. B* **82**, 075106 (2010).

15. Dzero, M., Sun, K., Galitski, V. & Coleman, P. Topological Kondo insulators. *Phys. Rev. Lett.* **104**, 106408 (2010).

16. Schaffer, R., Lee, E. K.-H., Yang, B.-J. & Kim, Y. B. Recent progress on correlated electron systems with strong spin-orbit coupling. *Rep. Prog. Phys.* **79**, 094504 (2016).

17. Lai, H.-H., Grefe, S. E., Paschen, S. & Si, Q. Weyl-Kondo semimetal in heavy-fermion systems. *Proc. Natl. Acad. Sci. U.S.A.* **115**, 93–97 (2018).

18. Grefe, S. E., Lai, H.-H., Paschen, S. & Si, Q. Weyl-Kondo semimetals in nonsymmorphic systems. *Phys. Rev. B* **101**, 075138 (2020).

19. Grefe, S. E., Lai, H.-H., Paschen, S. & Si, Q. Extreme topological tunability of Weyl-Kondo semimetal to Zeeman coupling. *arXiv:2012.15841* .

20. Dzsaber, S., Prochaska, L., Sidorenko, A., Eguchi, G., Svagera, R., Waas, M., Prokofiev, A., Si, Q. & Paschen, S. Kondo insulator to semimetal transformation tuned by spin-orbit coupling. *Phys. Rev. Lett.* **118**, 246601 (2017).

21. Dzsaber, S., Yan, X., Taupin, M., Eguchi, G., Prokofiev, A., Shiroka, T., Blaha, P., Rubel, O., Grefe, S. E., Lai, H.-H., Si, Q. & Paschen, S. Giant spontaneous Hall effect in a nonmagnetic Weyl-Kondo semimetal. *Proc. Natl. Acad. Sci. U.S.A.* **118**, e2013386118 (2021).

22. Dzsaber, S., Zocco, D. A., McCollam, A., Weickert, F., McDonald, R., Taupin, M., Yan, X., Prokofiev, A., Tang, L. M. K., Vlaar, B., Winter, L. E., Jaime, M., Si, Q. & Paschen, S. Controlling electronic topology in a strongly correlated electron system. *arXiv:1906.01182* .

23. Asaba, T., Ivanov, V., Thomas, S. M., Savrasov, S. Y., Thompson, J. D., Bauer, E. D. & Ronning, F. Colossal anomalous Nernst effect in a correlated noncentrosymmetric kagome ferromagnet. *Sci. Adv.* **7**, eabf1467 (2021).

24. Kang, M., Ye, L., Fang, S., You, J.-S., Levitan, A., Han, M., Facio, J. I., Jozwiak, C., Bostwick, A., Rotenberg, E., Chan, M. K., McDonald, R. D., Graf, D., Kaznatcheev, K., Vescovo, E., Bell, D. C., Kaxiras, E., van den Brink, J., Richter, M., Prasad Ghimire, M., Checkelsky, J. G. & Comin, R. Dirac fermions and flat bands in the ideal kagome metal FeSn. *Nat. Mater.* **19**, 163 (2020).

25. Yao, M., Lee, H., Xu, N., Wang, Y., Ma, J., Yazyev, O., Xiong, Y., Shi, M., Aeppli, G. & Soh, Y. Switchable Weyl nodes in topological kagome ferromagnet Fe_3Sn_2. *arXiv:1810.01514* .

26. Morimoto, T. & Nagaosa, N. Weyl Mott insulator. *Sci. Rep.* **6**, 19853 (2016).

27. Wagner, N., Ciuchi, S., Toschi, A., Trauzettel, B. & Sangiovanni, G. Resistivity exponents in 3d Dirac semimetals from electron-electron interaction. *Phys. Rev. Lett.* **126**, 206601 (2021).

28. Lourenço, J. A. S., Eneias, R. L. & Pereira, R. G. Kondo effect in a $\mathcal{PT}$-symmetric non-hermitian hamiltonian. *Phys. Rev. B* **98**, 085126 (2018).

29. Ahamed, S., Moessner, R. & Erten, O. Why rare-earth ferromagnets are so rare: Insights from the p-wave kondo model. *Phys. Rev. B* **98**, 054420 (2018).

30. Jang, S., Kealhofer, R., John, C., Doyle, S., Hong, J.-S., Shim, J. H., Si, Q., Erten, O., Denlinger, J. D. & Analytis, J. G. Direct visualization of coexisting channels of interaction in cesb. *Science Advances* **5**, eaat7158 (2019).

31. Chiu, C.-K. & Schnyder, A. P. Classification of reflection-symmetry-protected topological semimetals and nodal superconductors. *Phys. Rev. B* **90**, 205136 (2014).

32. Bian, G., Chang, T.-R., Sankar, R., Xu, S.-Y., Zheng, H., Neupert, T., Chiu, C.-K., Huang, S.-M., Chang, G., Belopolski, I., Sanchez, D. S., Neupane, M., Alidoust, N., Liu, C., Wang, B., Lee, C.-C., Jeng, H.-T., Zhang, C., Yuan, Z., Jia, S., Bansil, A., Chou, F., Lin, H. & Hasan, M. Z. Topological nodal-line fermions in spin-orbit metal $\mathrm{PbTaSe_2}$. *Nat. Commun.* **7**, 10556 (2016).

33. Bian, G., Chang, T.-R., Zheng, H., Velury, S., Xu, S.-Y., Neupert, T., Chiu, C.-K., Huang, S.-M., Sanchez, D. S., Belopolski, I., Alidoust, N., Chen, P.-J., Chang, G., Bansil, A., Jeng, H.-T., Lin, H. & Hasan, M. Z. Drumhead surface states and topological nodal-line fermions in $\mathrm{TlTaSe_2}$. *Phys. Rev. B* **93**, 121113 (2016).

34. Chan, Y.-H., Chiu, C.-K., Chou, M. Y. & Schnyder, A. P. $\mathrm{Ca_3P_2}$ and other topological semimetals with line nodes and drumhead surface states. *Phys. Rev. B* **93**, 205132 (2016).

35. Young, S. M. & Kane, C. L. Dirac semimetals in two dimensions. *Phys. Rev. Lett.* **115**, 126803 (2015).

36. Schoop, L. M., Ali, M. N., Straßer, C., Topp, A., Varykhalov, A., Marchenko, D., Duppel, V., Parkin, S. S. P., Lotsch, B. V. & Ast, C. R. Dirac cone protected by non-symmorphic symmetry and three-dimensional Dirac line node in ZrSiS. *Nat. Commun.* **7**, 11696 (2016).

37. Schoop, L. M., Topp, A., Lippmann, J., Orlandi, F., Müchler, L., Vergniory, M. G., Sun, Y., Rost, A. W., Duppel, V., Krivenkov, M., Sheoran, S., Manuel, P., Varykhalov, A., Yan, B., Kremer, R. K., Ast, C. R. & Lotsch, B. V. Tunable Weyl and Dirac states in the nonsymmorphic compound CeSbTe. *Sci. Adv.* **4**, eaar2317 (2018).

38. Muechler, L., Topp, A., Queiroz, R., Krivenkov, M., Varykhalov, A., Cano, J., Ast, C. R. & Schoop, L. M. Modular arithmetic with nodal lines: Drumhead surface states in ZrSiTe. *Phys. Rev. X* **10**, 011026 (2020).

39. Klemenz, S., Schoop, L. & Cano, J. Systematic study of stacked square nets: From Dirac fermions to

material realizations. *Phys. Rev. B* **101**, 165121 (2020).

40. Nica, E. M., Yu, R. & Si, Q. Glide reflection symmetry, Brillouin zone folding, and superconducting pairing for the $P4/nmm$ space group. *Phys. Rev. B* **92**, 174520 (2015).

41. Li, C., Wang, C. M., Wan, B., Wan, X., Lu, H.-Z. & Xie, X. C. Rules for phase shifts of quantum oscillations in topological nodal-line semimetals. *Phys. Rev. Lett.* **120**, 146602 (2018).

42. Yang, H., Moessner, R. & Lim, L.-K. Quantum oscillations in nodal line systems. *Phys. Rev. B* **97**, 165118 (2018).

43. Kwan, Y. H., Reiss, P., Han, Y., Bristow, M., Prabhakaran, D., Graf, D., McCollam, A., Parameswaran, S. A. & Coldea, A. I. Quantum oscillations probe the fermi surface topology of the nodal-line semimetal CaAgAs. *Phys. Rev. Research* **2**, 012055 (2020).

44. Stuart, B. A., Choi, S., Kim, J., Muechler, L., Queiroz, R., Oudah, M., Schoop, L. M., Bonn, D. A. & Burke, S. A. Quasiparticle interference observation of the topologically nontrivial drumhead surface state in ZrSiTe. *Phys. Rev. B* **105**, L121111 (2022).

45. Biderang, M., Leonhardt, A., Raghuvanshi, N., Schnyder, A. P. & Akbari, A. Drumhead surface states and their signatures in quasiparticle scattering interference. *Phys. Rev. B* **98**, 075115 (2018).

46. Kirchner, S., Paschen, S., Chen, Q., Wirth, S., Feng, D., Thompson, J. D. & Si, Q. Colloquium: Heavy-electron quantum criticality and single-particle spectroscopy. *Rev. Mod. Phys.* **92**, 011002 (2020).

47. Anand, V. K., Adroja, D. T., Bhattacharyya, A., Klemke, B. & Lake, B. Kondo lattice heavy fermion behavior in $\mathrm{CeRh_2Ga_2}$. *J. Phys. Condens. Matter* **29**, 135601 (2017).

48. Gignoux, D., Schmitt, D., Zerguine, M., Ayache, C. & Bonjour, E. Magnetic properties of a new Kondo lattice compound: $\mathrm{CePt_2Si_2}$. *Phys. Lett. A* **117**, 145–149 (1986).

49. Nakamoto, G., Takabatake, T., Fujii, H., Minami, A., Maezawa, K., Oguro, I. & Menovsky, A. Crystal growth and characterization of the Kondo semimetal CeNiSn. *J. Phys. Soc. Jpn.* **64**, 4834–4840 (1995).

50. Galadzhun, Y. V., Hoffmann, R.-D., Pöttgen, R. & Adam, M. Complex three-dimensional $\mathrm{Au_3In_5}$ polyanions in $\mathrm{Ln_2Au_3In_5}$ ($\mathrm{Ln} = \mathrm{Ce}, \mathrm{Pr}, \mathrm{Nd}, \mathrm{Sm}$). *J. Solid State Chem.* **148**, 425–432 (1999).

51. Aeppli, G. & Fisk, Z. Kondo insulators. *Comm. Condemns. Matter Phys.* **16**, 155 (1992).

52. Nikolić, P. Two-dimensional heavy fermions on the strongly correlated boundaries of Kondo topological insulators. *Phys. Rev. B* **90**, 235107 (2014).

53. Yu, R. & Si, Q. Orbital-selective mott phase in multiorbital models for iron pnictides and chalcogenides. *Phys. Rev. B* **96**, 125110 (2017).

54. Komijani, Y. & Kotliar, G. Analytical slave-spin mean-field approach to orbital selective mott insula-

tors. *Phys. Rev. B* **96**, 125111 (2017).

55. Huang, J., Yu, R., Xu, Z., Zhu, J.-X., Oh, J. S., Jiang, Q., Wang, M., Wu, H., Chen, T., Denlinger, J. D., Mo, S.-K., Hashimoto, M., Michiardi, M., Pedersen, T. M., Gorovikov, S., Zhdanovich, S., Damascelli, A., Gu, G., Dai, P., Chu, J.-H., Lu, D., Si, Q., Birgeneau, R. J. & Yi, M. Correlation-driven electronic reconstruction in $FeTe_{1-x}Se_x$. *Commun. Phys.* **5**, 29 (2022).

56. Song, Z.-D. & Bernevig, B. A. Matbg as topological heavy fermion: I. exact mapping and correlated insulators. *arXiv preprint arXiv:2111.05865* (2021).

57. Hu, H., Chen, L., Setty, C., Grefe, S. E., Prokofiev, A., Kirchner, S., Paschen, S., Cano, J. & Si, Q. Gapless electronic topology without free-electron counterpart. *arXiv:2110.06182* (2021).

58. Wu, W., Jiao, Y., Li, S., Sheng, X.-L., Yu, Z.-M. & Yang, S. A. Hourglass Weyl loops in two dimensions: Theory and material realization in monolayer $GaTeI$ family. *Phys. Rev. Materials* **3**, 054203 (2019).

59. Bhattacharjee, A., Coqblin, B., Raki, M., Forro, L., Ayache, C. & Schmitt, D. Anisotropy of transport properties in the Kondo compound $CePt_2Si_2$: experiments and theory. *J. Phys. (Paris)* **50**, 2781–2793 (1989).

60. Kresse, G. & Hafner, J. Ab initio molecular dynamics for open-shell transition metals. *Phys. Rev. B* **48**, 13115–13118 (1993).

61. Kresse, G. & Furthmüller, J. Efficiency of ab-initio total energy calculations for metals and semiconductors using a plane-wave basis set. *Comput. Mater. Sci.* **6**, 15–50 (1996).

62. Perdew, J. P., Burke, K. & Ernzerhof, M. Generalized gradient approximation made simple. *Phys. Rev. Lett.* **77**, 3865–3868 (1996).

63. Kresse, G. & Joubert, D. From ultrasoft pseudopotentials to the projector augmented-wave method. *Phys. Rev. B* **59**, 1758–1775 (1999).

64. Hobbs, D., Kresse, G. & Hafner, J. Fully unconstrained noncollinear magnetism within the projector augmented-wave method. *Phys. Rev. B* **62**, 11556–11570 (2000).

65. Nesterenko, S., Avzuragova, V., Tursina, A. & Kaczorowski, D. Structural peculiarities and magnetic properties of a novel cerium gallide $CeRh_2Ga_2$. *J. Alloys Compd.* **717**, 136–140 (2017).

66. Herath, U., Tavadze, P., He, X., Bousquet, E., Singh, S., Muñoz, F. & Romero, A. H. Pyprocar: A python library for electronic structure pre/post-processing. *Computer Physics Communications* **251**, 107080 (2020).

Acknowledgments

Work at Rice has been supported by the Air Force Office of Scientific Research under Grant No. FA9550-21-1-0356 (C.S. and Q.S.), the National Science Foundation under Grant No. DMR-2220603 (L.C.) and the Robert A. Welch Foundation Grant No. C-1411 (H.H.). The majority of the computational calculations have been performed on the Shared University Grid at Rice funded by NSF under Grant EIA-0216467, a partnership between Rice University, Sun Microsystems, and Sigma Solutions, Inc., the Big-Data Private-Cloud Research Cyberinfrastructure MRI-award funded by NSF under Grant No. CNS-1338099, and the Extreme Science and Engineering Discovery Environment (XSEDE) by NSF under Grant No. DMR170109. M.G.V. acknowledges the support from the Spanish Ministry of Science and Innovation Grant No. PID2019-109905GB-C21 and the Deutsche Forschungsgemeinschaft (DFG, German Research Foundation) GA 3314/1-1 – FOR 5249 (QUAST). Work at Los Alamos was carried out under the auspices of the U.S. Department of Energy (DOE) National Nuclear Security Administration under Contract No. 89233218CNA000001, and was supported by LANL LDRD Program. J.C. acknowledges the support of the National Science Foundation under Grant No. DMR-1942447 and the support of the Flatiron Institute, a division of the Simons Foundation. Work in Vienna was supported by the Austrian Science Fund (projects No. 29279-N27 and I 5868-N - FOR 5249 - QUAST). Four of us (S.G., S. P., J. C. and Q.S.) acknowledge the hospitality of the Aspen Center for Physics, which is supported by NSF grant No. PHY-1607611.

Author contributions

Q.S., J.C. and S. P. conceived the research. L.C., C.S., H.H., S.E.G., J.C. and Q.S. carried out theoretical model studies. A.P. and S.P. identified candidate materials for the proposed correlated topological semimetals. L.F. and X.Y. synthesized the material and G.E. performed the specific heat measurements. M.G.V. performed DFT calculations. L.C., C.S., H.H., J.C. and Q.S. wrote the manuscript, with inputs from all authors.

Competing interests

The authors declare no competing interests.

Additional information

Correspondence and requests for materials should be addressed to Q.S. (qmsi@rice.edu), J.C. (jennifer.cano@stonybrook.edu) and S.P. (paschen@ifp.tuwien.ac.at)

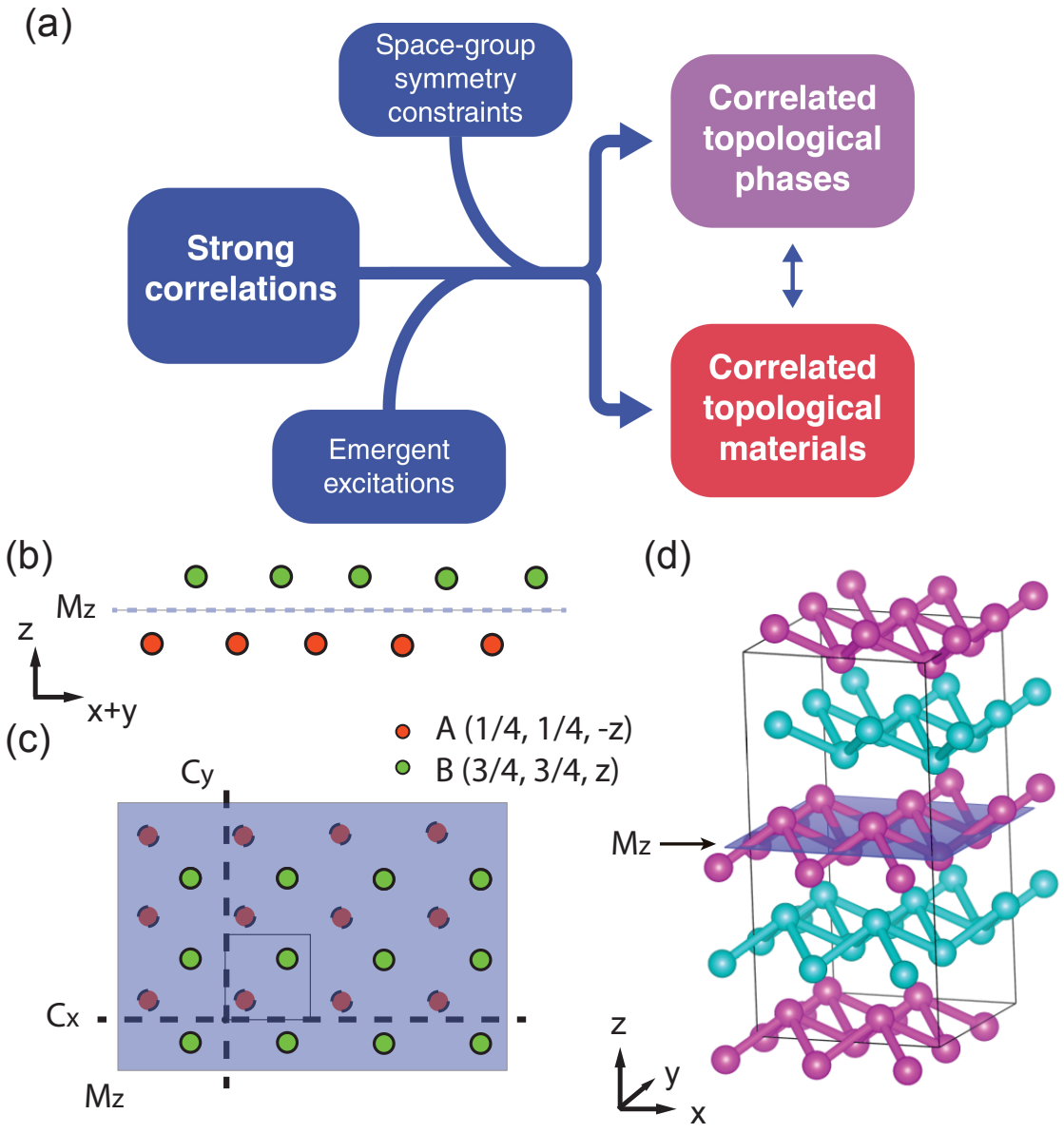


FIG. 1. **Materials design principle and space-group symmetry. a,** The proposed cooperation between strong correlations and space-group symmetry in realizing correlated gapless topological states and materials. Here, low-energy excitations emerge from strong correlations and are subjected to space-group symmetry constraints, leading to correlated topological phases in theoretical models and materials that realize such phases. **b, c,** The lattice structure of the square-net layer with sublattices A, B on Wyckoff position $2c$. Also shown are the mirror (M_z) and screw (C_x and C_y) nonsymmorphic symmetries. **d,** $\mathcal{AA}$ stacking of the square-net layers into a 3D structure.

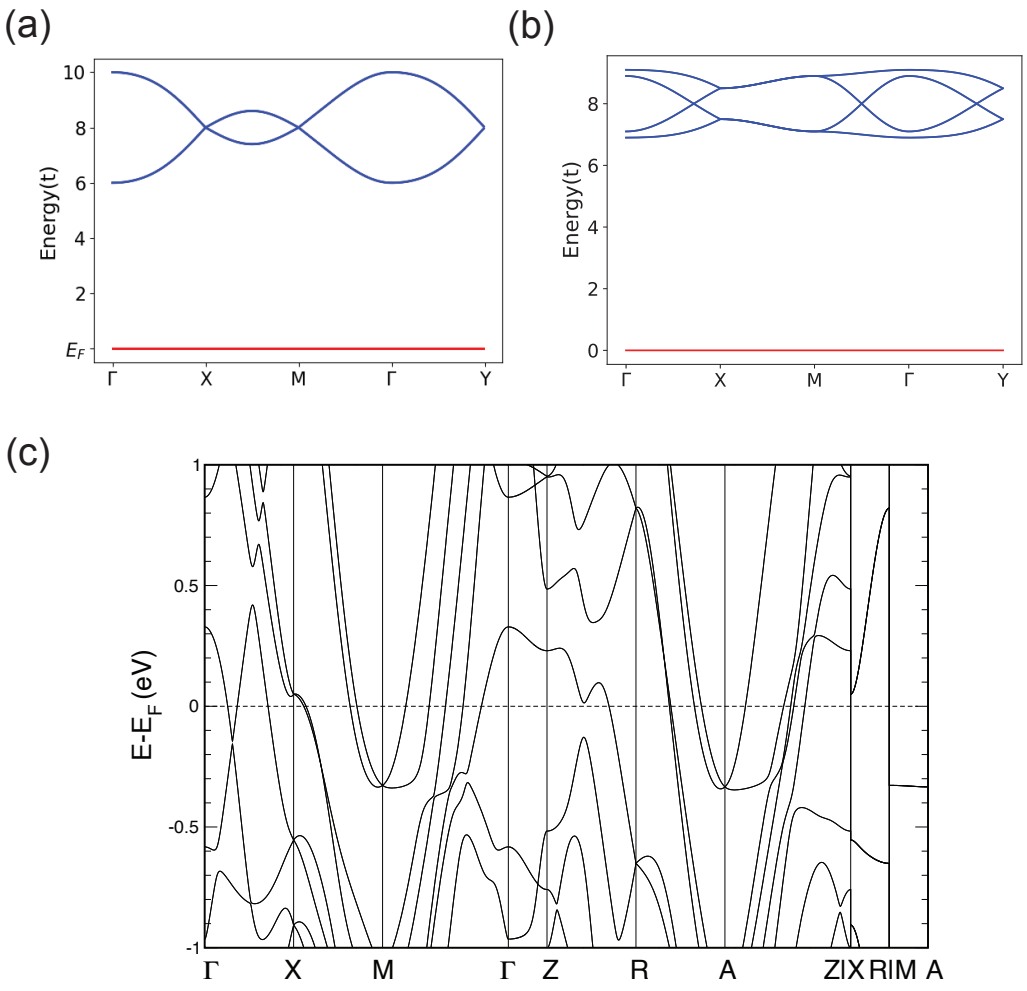


FIG. 2. **Electronic structure in the absence of Kondo effect. a,** Dispersion of a 2D square net with (t_1, t_2, t^{SO}) = $(1, 0, 0.6)$). The line at E_F illustrates the localized electrons. The four-fold degeneracies of the conduction bands occur at high symmetry points X, Y, M away from the Fermi energy. **b,** Dispersion of the 3D-stacked square net without either inversion symmetry breaking or SOC. The parameters are $(t_1, t_2, t_z^1, t_z^2, \Delta_z)$ = $(1, 0.4, 0.3, 0.3, 0.8)$. **c,** Bandstructure of the conduction spd-electrons of $CePt_2Si_2$, as determined by f-core DFT calculations. Symmetry-dictated Dirac nodes appear at X and M (and R and A) away from the Fermi energy, as captured by the model dispersions of **a** and **b**.

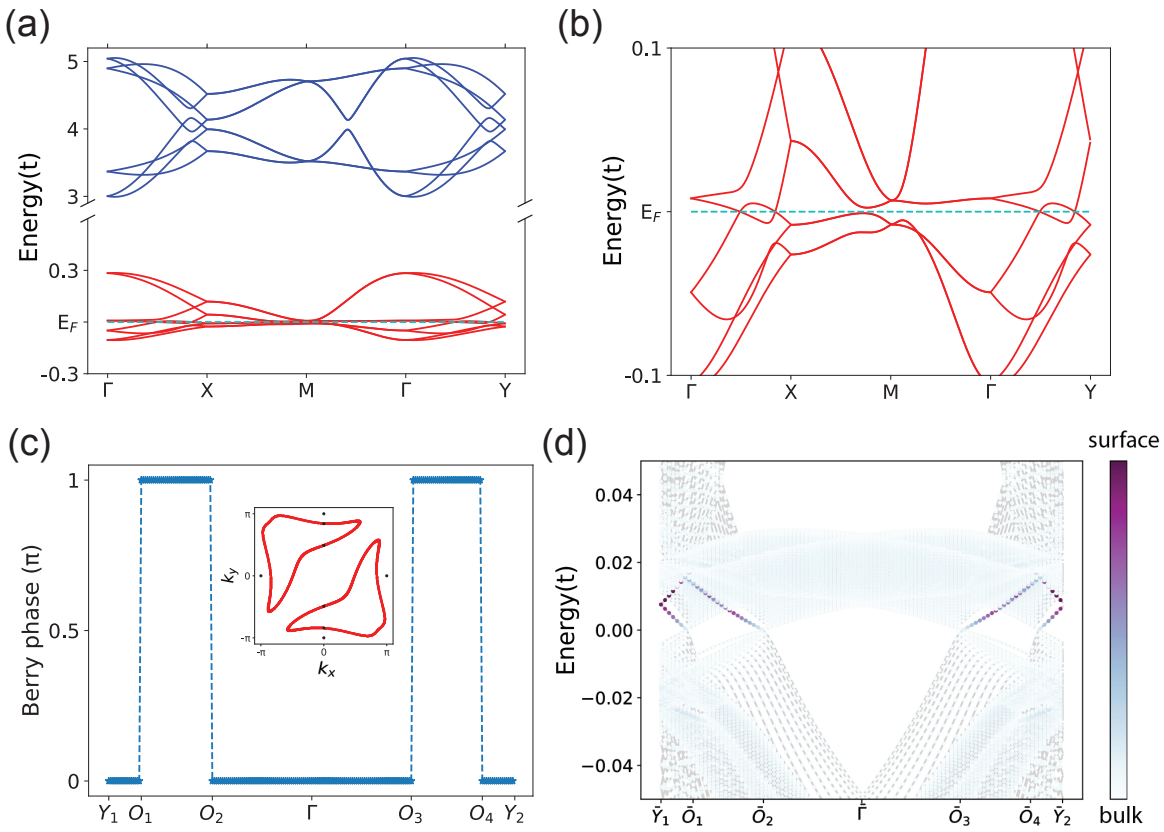


FIG. 3. **Kondo-driven composite fermions of 3D stacked square-nets with broken inversion symmetry. a,** The dispersion, including for the composite fermions (the lower red part), within the $k_z = 0$ plane. Here $V = 3$, in unit of t_1 that is set to 1. The other parameters are set to $(t_2, \Delta, t_z^1, t_z^2, \Delta_z, m_z, E_d, \mu) = (0.4, 0.4, 0.3, 0.3, 0.8, 0.08, -2, -3.730)$. The parameters were chosen without any fine-tuning; the only requirement is that r_1 and r_2 are found to be nonzero. The saddle-point analysis yields $(r_1, r_2, l_1, l_2) = (0.498, 0.374, -2.820, -2.294)$. **b,** The zoomed-in dispersion of the Kondo-driven composite fermions. **c,** The Berry phase (in the z-direction) of the Kondo-driven Weyl nodal lines for fixed $k_x = 0$; $O_{1,2,3,4}$ mark the points of intersection with the nodal lines [Fig. S3(c)]. Inset: the Kondo-driven Weyl nodal lines in the $k_z = 0$ plane. **d,** Kondo driven drumhead surface states. Shown here is the momentum-resolved surface density of states for the spectrum close to Fermi energy on the (001) surface along $Y_1(0, -\pi)$ to $Y_2(0, \pi)$. A bar atop a momentum represents its projection onto the surface.

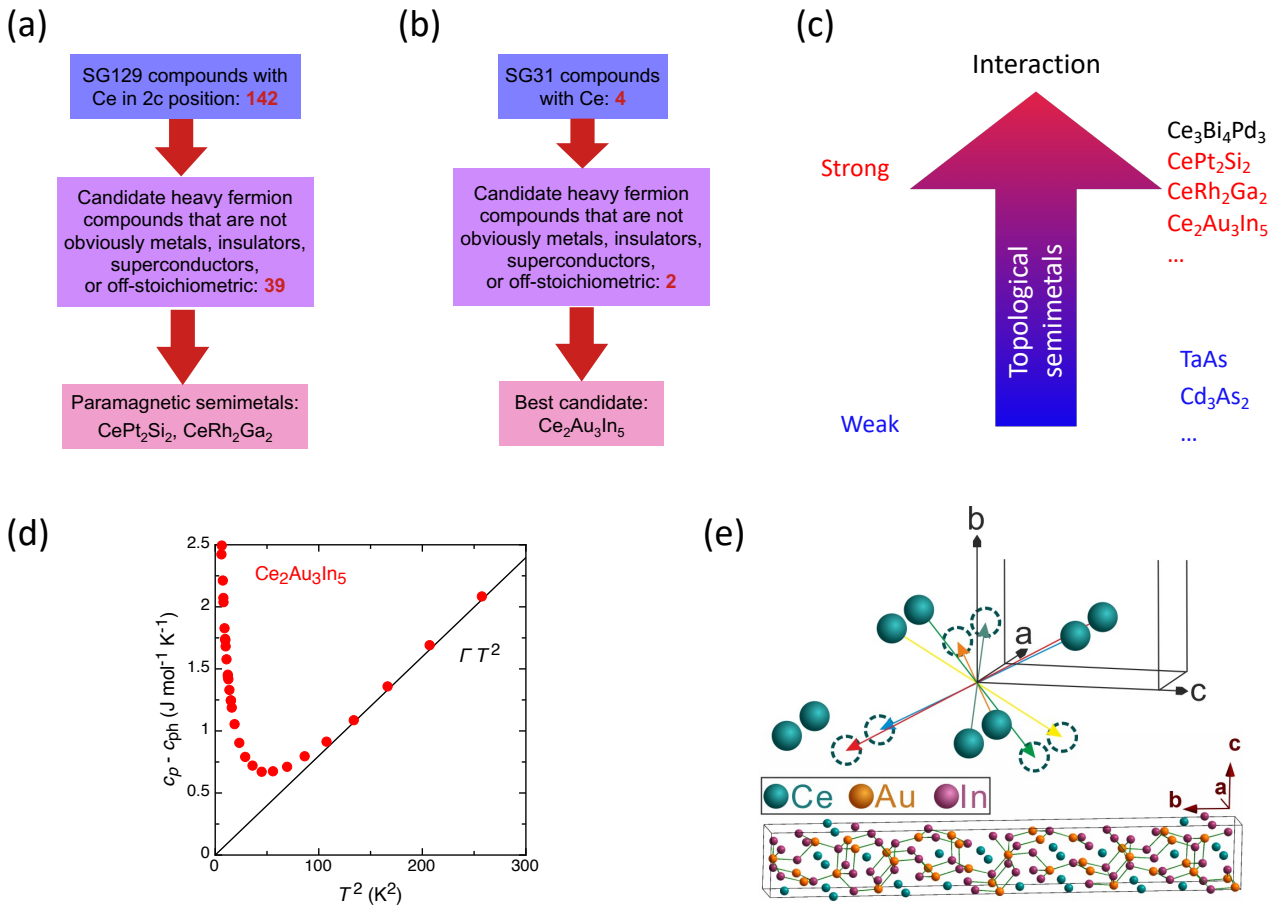


FIG. 4. **Design of new materials for correlation-driven topological semimetal phases and the first synthesized material.** The design procedure as applied to SG 129 with Ce-ions on the Wyckoff position 2c (**a**) and to SG 31 (**b**). The 39 compounds of the middle box in **a** and the 4 compounds of **b** are given in the Supplementary Information (Fig. S4). **c,** Summary of the newly identified candidate materials (red) for correlation-driven topological semimetals based on the search in **a** and **b** and their placement along the correlation axis. **d,** Electronic specific heat, $c_p - c_{ph}$, as a function of T^2. In the paramagnetic regime sufficiently above the low-temperature upturn (possibly a tail of a lower-lying magnetic phase transition), a ΓT^2 form is observed. **e.** Crystal structure of $Ce_2Au_3In_5$ and illustration of its inversion-symmetry breaking.

Methods

The periodic Anderson model, solution method and symmetry analyses The PAM is specified by Eq. 1. The model contains two species of spin-$1/2$ electrons. The Hamiltonian $\mathcal{H}_d$, containing spin-$1/2$ d-operators, describes the physical localized f electrons:

$$\mathcal{H}_d = E_d \sum_{i,\sigma} d^\dagger_{i\sigma} d_{i\sigma} + U \sum_i n^d_{i\uparrow} n^d_{i\downarrow} \,, \tag{3}$$

with the energy level E_d and onsite Coulomb repulsion U. Whereas $\mathcal{H}_c$, involving c-operators, characterizes the spd conduction electrons that form the noninteracting bands. The hybridization term, which describes the Kondo coupling between the conduction and f- electrons, is given by

$$\mathcal{H}_{cd} = V \sum_{i\sigma} \left(d^\dagger_{i\sigma} c_{i\sigma} + h.c. \right) \,, \tag{4}$$

where V represents the hybridization between the two species of electrons. The following features of the symmetry group 129 and model justify its application to many f-electron materials in this space group. The symmetry representations of this space group are such that at each high-symmetry point, the degeneracy of the bands is independent of the symmetry of the orbital (assuming spin-orbit coupling). Thus, our model applies regardless of the nature of the orbitals near the Fermi energy. The dispersion of the Kondo-driven composite fermions stays near the Fermi energy, within the Kondo energy. Thus, while we specialize in the quarter-filled case, corresponding to one electron per site, changing the filling will only shift the composite-fermion bands up to the Kondo energy. The saddle-point analysis, involving self-consistent equations that are exact in a large-N limit (where N is the spin degeneracy), is described in the Supplementary Information (SI). The Kondo effect generates composite fermions that must be located near the Fermi energy. While we will describe symmetry constraints in terms of the dispersion of the composite fermions, the same conclusion is reached through a more general analysis that is carried out in terms of the eigenvectors of the full single-particle Green's function for the interacting Hamiltonian[57] (see SI).

The PAM in 2D involves $\mathcal{H}_c = \sum_{\mathbf{k}} \Psi^\dagger_{\mathbf{k}} H_c(\mathbf{k}) \Psi_{\mathbf{k}}$, where $\Psi^T_{\mathbf{k}} = (c_{\mathbf{k}\uparrow A}, c_{\mathbf{k}\downarrow A}, c_{\mathbf{k}\uparrow B}, c_{\mathbf{k}\downarrow B})$, and

$$\begin{aligned} H_c(\mathbf{k}) =& t_1 \cos\frac{k_x}{2} \cos\frac{k_y}{2} \tau_x + t_2(\cos k_x + \cos k_y) + t^{SO}(\sin k_x \sigma_y - \sin k_y \sigma_x)\tau_z \\ &+ \Delta \sin(\frac{k_x - k_y}{2})\tau_x \sigma_z, \end{aligned} \tag{5}$$

where $\tau = (\tau_x, \tau_y, \tau_z)$'s and $\sigma = (\sigma_x, \sigma_y, \sigma_z)$'s are Pauli matrices acting on the (A,B) sublattice and spin spaces respectively. A more explicit form of the Hamiltonian can be found in the SI. For

definiteness, we consider the lattice model with tight-binding hopping terms between the nearest (t_1) and next-nearest (t_2) sites [as illustrated in the SI, Fig. S3(a)], an SOC (t^{SO}) term, and an inversion-symmetry-breaking (Δ) term. The first three terms contain all the symmetry-allowed components up to the next-nearest neighbor, describing an effective s-orbital model on Wyckcoff position $2c$ with both time reversal symmetry ($\mathcal{T}$) and inversion symmetry ($\mathcal{I}$). The presence of both $\mathcal{T}$ and $\mathcal{I}$ ensure each band is doubly degenerate with states $|g\rangle$ and $\mathcal{TI}|g\rangle$. In addition, the symmetries include the glide mirror symmetry $\{M_z|\frac{1}{2}\frac{1}{2}\}$ (Fig. 1(b)(c))) and two screw symmetries $\{C_{2x}|\frac{1}{2}0\}$ and $\{C_{2y}|0\frac{1}{2}\}$ (where $\{C_{ni}|\mathfrak{t}\}$ = n-fold rotation along axis i + fractional translation $\mathfrak{t}$ as depicted in Fig. 1(c)). The bands are generically two-fold degenerate. However, a four-fold degeneracy at X arises as a result of either the mirror nonsymmorphic $\{M_z|\frac{1}{2}\frac{1}{2}\}$ symmetry or the screw nonsymmorphic $\{C_{2x}|\frac{1}{2}0\}$ symmetry. The same degeneracy appears at Y, due to either the mirror nonsymmorphic $\{M_z|\frac{1}{2}\frac{1}{2}\}$ symmetry or the screw nonsymmorphic $\{C_{2y}|0\frac{1}{2}\}$ symmetry. Finally, a four-fold degeneracy also develops at M, from either the $\{C_{2x}|\frac{1}{2}0\}$ or the $\{C_{2y}|0\frac{1}{2}\}$ symmetry. The fourth term has the form of $\Delta\sin(\frac{k_x-k_y}{2})\tau_x\sigma_z$. It breaks the inversion symmetry of $p4/nmm$, while preserving its mirror symmetry[35,58]. The quarter-filling case we examine corresponds to one electron per site. We consider the realistic regime of parameters corresponding to the limit of strong coupling, $U\to\infty$, and with the d-electron level being sufficiently deep compared to the energy of the conduction-electron bands (*i.e.*, for sufficiently negative E_d), in which the system is in the Kondo limit. The saddle-point results are compatible with those derived from a variety of other methods. For example, the Kondo effect is found to develop only when the hybridization strength goes above a threshold value. This reflects the fact that the bare conduction-electron bath has a gap near the Fermi energy. The gap makes the Kondo coupling to be irrelevant (as opposed to marginally relevant) in the renormalization-group sense; as a result, a nonzero threshold value of the Kondo coupling or hybridization is needed for the Kondo effect to develop.

We now specify the PAM in 3D. Here, $\mathcal{H}_d$ and $\mathcal{H}_{cd}$ are the same (except that the site summation is in the 3D lattice). For the conduction electrons, the Hamiltonian now takes the form: $\mathcal{H}_c^{3D}=\sum_{\mathbf{k}}\Phi_{\mathbf{k}}^\dagger H_c^{3D}(\mathbf{k})\Phi_{\mathbf{k}}$, where $\Phi_{\mathbf{k}}^T=(c^s_{\mathbf{k}\uparrow A},c^s_{\mathbf{k}\downarrow A},c^s_{\mathbf{k}\uparrow B},c^s_{\mathbf{k}\downarrow B},c^p_{\mathbf{k}\uparrow A},c^p_{\mathbf{k}\downarrow A},c^p_{\mathbf{k}\uparrow B},c^p_{\mathbf{k}\downarrow B})$. In this equation,

$$H_c^{3D}(\mathbf{k})=H_c(k_x,k_y)\otimes\rho_z+\Delta_z\rho_z+t_z^1\sin(\frac{k_z}{2})\rho_y+t_z^2\cos(k_z)\rho_z+m_z\tau_x\otimes\sigma_x\otimes\rho_y\,, \qquad (6)$$

with $\rho_{x,y,z}$ being the Pauli matrices in the space of the two stacking layers (see the SI for a more explicit form of the Hamiltonian). Here, the third and the fourth terms represent the nearest- and next-nearest-neighbor hoppings along the z-direction [as illustrated in the SI, Fig. S3(a)] and the

fifth term is the SOC along the z-direction. For simplicity, we have chosen an s- and p-orbital stacking and set the s and p orbitals to couple with the d-electrons with the same hybridization strength. However, the nature of the resulting topological semimetal phase is determined by the underlying space-group symmetry and is generic to the given SG. Further details of our analysis is described in the SI. Again we focus on the quarter-filling case.

Crystal growth and specific heat of $Ce_2Au_3In_5$ and $La_2Au_3In_5$ Single crystals of $Ce_2Au_3In_5$ were grown from In flux using alumina crucibles. Elements of high purity ($>99.9\%$) were taken for the synthesis. Single crystals were separated from the melt by centrifuging. Attempts to prepare by this way single crystals of $La_2Au_3In_5$ failed. A single phase polycrystalline $La_2Au_3In_5$ sample was prepared by melting pure elements in the stoichiometric ratio in a high frequency furnace and annealing the as cast sample at $650°$C for three days. All samples were analysed by x-ray powder diffraction and energy dispersive x-ray spectroscopy (EDX) for phase purity and composition prior to the physical property measurements. The single crystallinity of the $Ce_2Au_3In_5$ samples was checked by Laue x-ray measurements. The specific heat c_p was measured using the Quantum Design heat capacity option for the PPMS. Figure S6(a) shows the c_p of $Ce_2Au_3In_5$ and $La_2Au_3In_5$ as a function of T^3. The phonon contribution to the specific heat c_{ph}, assumed as usual to be the same for both compounds, was estimated from the c_p of $La_2Au_3In_5$ by subtracting its electronic contribution, determined as follows: The c_p/T of $La_2Au_3In_5$ at low temperatures (<5 K) is well described by a conventional Debye-Sommerfeld model, $c_p/T = \gamma + \beta T^2$. It yielded a finite electronic specific heat coefficient $\gamma = (16.2\pm0.6)$ mJ/mol K^2 and a β value that corresponds to the Debye temperature (232 ± 5) K. The electronic specific heat of $Ce_2Au_3In_5$ was obtained by subtracting this c_{ph} from its total c_p.

f-core DFT calculations The electronic structure calculations were performed with the f states removed from the pseudo-potential to model the band structure. The SOC was taken into account. Further details can be found in the SI.

Data availability The data that support the findings of this study are available from the corresponding author upon reasonable request.

Supplementary Information

Kondo-driven topological semimetals in 2D

The Kondo effect leads to composite fermions near the Fermi energy. For the inversion-symmetric case ($\Delta = 0$), the renormalized dispersion as shown in Fig. S1(a) was already discussed in the main text. For the case with broken inversion symmetry (i.e., with nonzero Δ), we show the renormalized dispersion in Fig. S1(b). The four-fold degenerate states at X and Y are split into two pairs of two-fold Weyl nodes above and below the Fermi energy. The different branches of the Weyl nodes cross each other at the Fermi energy, giving rise to Fermi-energy-bound Weyl-nodal lines, as shown in Fig. S1(c). The Weyl-nodal lines are protected by the mirror nonsymmorphic symmetry[35,58]. We note that, here too, the Kondo-driven nodal lines have been identified in the presence of SOC.

Kondo-driven topological semimetals for SG 129

Utilizing the 2D model as the building block, we consider how the Kondo-driven topological nodes develop in the SG 129 case. This can already be done with a direct stacking along the z-direction. As shown in Fig. S2(a), the symmetry enforced Dirac points at high symmetry points in 2D is extended along z-direction and becomes Dirac nodal lines along the high symmetry hinges; the degree of their dispersion is related to the strength of the z-direction hoppings. Thus, there could only be Dirac points that cross the Fermi energy [Fig. S2(b)]. In the presence of a ferromagnetic order or Zeeman coupling from an external magnetic field, the Dirac nodes are turned into Weyl nodes. In addition, pairs of Weyl nodes can in principle appear along $\Gamma - X/Y/Z$, which are protected by rotational symmetries according to magnetic group analysis. This is illustrated in Fig. S2(c)(d), which show a pair of Weyl nodes along $\Gamma - Z$.

Additional data for the Kondo-driven nodal line in 3D

In Fig. 3 of the main text, we showed the renormalized electronic structure for the 3D square net along high-symmetry directions within the $k_z = 0$ plane. Here, we plot the bands along high-symmetry directions in the entire 3D Brillouin zone. The renormalized band structure is shown in Fig. S3(a) along the path connecting high symmetry points as can be seen through Fig. S3(b). Except for the Weyl line in the $k_z = 0$ plane, the heavy bands are fully gapped across the 3D Brillouin zone.

Hamiltonians in matrix form

Consider first the 2D case. The Hamiltonian of the conduction c-fermion, $\mathcal{H}_c$, is described in a

matrix form: $\mathcal{H}_c = \sum_{\mathbf{k}} \Psi^\dagger_{\mathbf{k}} H_c(\mathbf{k}) \Psi_{\mathbf{k}}$, where $\Psi^T_{\mathbf{k}} = (c_{\mathbf{k}\uparrow A}, c_{\mathbf{k}\downarrow A}, c_{\mathbf{k}\uparrow B}, c_{\mathbf{k}\downarrow B})$, with A and B being the two sublattices, $\mathbf{k}$ the wavevector, and $\sigma = \uparrow, \downarrow$ marking the spin quantum numbers.

$$H_c(\mathbf{k}) = \begin{pmatrix} f_2(\mathbf{k}) & f_{SO}(\mathbf{k}) & f_1(\mathbf{k}) + f_\Delta(\mathbf{k}) & 0 \\ f_{SO}(\mathbf{k}) & f_2(\mathbf{k}) & 0 & f_1(\mathbf{k}) - f_\Delta(\mathbf{k}) \\ f_1(\mathbf{k}) + f_\Delta(\mathbf{k}) & 0 & f_2(\mathbf{k}) & -f_{SO}(\mathbf{k}) \\ 0 & f_1(\mathbf{k}) - f_\Delta(\mathbf{k}) & -f_{SO}(\mathbf{k}) & f_2(\mathbf{k}) \end{pmatrix}$$

with

$$\begin{aligned} f_1(\mathbf{k}) &= t_1 \cos\frac{k_x}{2} \cos\frac{k_y}{2}, \\ f_2(\mathbf{k}) &= t_2(\cos k_x + \cos k_y), \\ f_{SO}(\mathbf{k}) &= t^{SO}(-\sin k_y - i \sin k_x), \\ f_\Delta(\mathbf{k}) &= \Delta \sin(\frac{k_x - k_y}{2}), \end{aligned}$$

where t_1/t_2 are the nearest and next-nearest neighbor hopping parameters, t^{SO} is the symmetry-allowed SOC and Δ breaks the inversion symmetry.

Consider next the Hamiltonian for the 3D model. For the conduction c-fermions, the Hamiltonian now takes the form: $\mathcal{H}^{3D}_c = \sum_{\mathbf{k}} \Phi^\dagger_{\mathbf{k}} H^{3D}_c(\mathbf{k}) \Phi_{\mathbf{k}}$, where $\Phi^T_{\mathbf{k}} = (c^s_{\mathbf{k}\uparrow A}, c^s_{\mathbf{k}\downarrow A}, c^s_{\mathbf{k}\uparrow B}, c^s_{\mathbf{k}\downarrow B}, c^p_{\mathbf{k}\uparrow A}, c^p_{\mathbf{k}\downarrow A}, c^p_{\mathbf{k}\uparrow B}, c^p_{\mathbf{k}\downarrow B})$. And

$$H^{3D}_c(\mathbf{k}) = \begin{pmatrix} H_c(k_x, k_y) + H_z(k_z) & \rho(k_z) \\ \rho^\dagger(k_z) & -H_c(k_x, k_y) - H_z(k_z) \end{pmatrix},$$

where

$$H_z(k_z) = (\Delta_z + t_z^2 \cos k_z) \mathbb{1}_{4\times 4},$$

and

$$\rho(k_z) = \begin{pmatrix} -it_z^1 \sin\frac{k_z}{2} & & & -im_z \\ & -it_z^1 \sin\frac{k_z}{2} & -im_z & \\ & -im_z & -it_z^1 \sin\frac{k_z}{2} & \\ -im_z & & & -it_z^1 \sin\frac{k_z}{2} \end{pmatrix}.$$

Here, Δ_z is the chemical potential difference between two layers, t_z^1/t_z^2 represent the nearest- and next-nearest-neighbor hoppings along the z-direction and m_z is the SOC along z-direction.

Saddle point equations

We describe the auxiliary-boson method in this section. In the 2D square-net model, we first fix the electron filling to be one per site

$$n_d + n_c = 1\,, \tag{S1}$$

with

$$n_d = \tfrac{1}{N_\mathrm{u}} \textstyle\sum_{i,\sigma} d^\dagger_{i\sigma} d_{i\sigma} \,, \tag{S2}$$

$$n_c = \tfrac{1}{N_\mathrm{u}} \textstyle\sum_{i,\sigma} c^\dagger_{i\sigma} c_{i\sigma} \,, \tag{S3}$$

where N_u counts the total number of sites.

In the infinite-U limit, the localized d-electrons can be represented as $d^\dagger_{i\sigma} = b_i f^\dagger_{i\sigma}$ with local constraint

$$b^\dagger_i b_i + \sum_\sigma f^\dagger_{i\sigma} f_{i\sigma} = 1 \,. \tag{S4}$$

This constraint rules out the double occupancy entirely. At the saddle point, the auxiliary bosons condense, with $b_i \to \langle b_i \rangle = r$. We further introduce a uniform Lagrangian multiplier l to enforce the local constraint in Eq. S4, which gives rise to the saddle-point Hamiltonian:

$$\mathcal{H}_s = \mathcal{H} + l \left(\frac{1}{N_\mathrm{u}} \sum_{i,\sigma} f^\dagger_{i\sigma} f_{i\sigma} + r^2 - 1 \right) - \mu \frac{1}{N_\mathrm{u}} \sum_{i,\sigma} n^c_{i\sigma}, \tag{S5}$$

where μ is the chemical potential. The saddle point equations are

$$\sum_\sigma \left(V \langle c^\dagger_\sigma f_\sigma \rangle + h.c. \right) - 2rl = 0 \,, \tag{S6}$$

$$\sum_\sigma \langle f^\dagger_\sigma f_\sigma \rangle - r^2 = 1 \,. \tag{S7}$$

Together with the filling constraint Eq. S1, we can self-consistently determine the variational parameters (μ, r, l).

We apply the same auxiliary-boson method to the 3D stacked square net with a saddle-point Hamiltonian

$$\begin{aligned} H = {} & H_c^{3D} + r_1 V \frac{1}{N_u} \sum_{i,\sigma} (s^\dagger_{i,\sigma} f^1_{i,\sigma} + h.c.) + E_d \frac{1}{N_u} \sum_{i,\sigma} f^{1\dagger}_{i,\sigma} f^1_{i,\sigma} \\ & + r_2 V \frac{1}{N_u} \sum_{i,\sigma} (p^\dagger_{i,\sigma} f^2_{i,\sigma} + h.c.) + E_d \frac{1}{N_u} \sum_{i,\sigma} f^{2\dagger}_{i,\sigma} f^2_{i,\sigma} \\ & + l_1 \frac{1}{N_u} \left(\sum_{i,\sigma} f^{1\dagger}_{i,\sigma} f^1_{i,\sigma} + r_1^2 - 1 \right) + l_2 \frac{1}{N_u} \left(\sum_{i,\sigma} f^{2\dagger}_{i,\sigma} f^2_{\sigma} + r_2^2 - 1 \right) \\ & - \mu \frac{1}{N_u} \sum_{i,\sigma} \left(s^\dagger_{i,\sigma} s_{i,\sigma} + p^\dagger_{i,\sigma} p_{i,\sigma} \right) , \end{aligned} \tag{S8}$$

where f^1_σ and f^2_σ, r_1 and r_2, l_1 and l_2 represent the auxiliary fermions, condensed auxiliary bosons and Lagrangian multipliers for each layer.

The saddle point equations are

$$\frac{1}{N_u}\sum_{\sigma}\left(V\langle s^{\dagger}_{\sigma}f^{1}_{\sigma}\rangle + h.c.\right) - 2r_1 l_1 = 0\,, \tag{S9}$$

$$\frac{1}{N_u}\sum_{\sigma}\langle f^{1\dagger}_{\sigma}f^{1}_{\sigma}\rangle - r_1^2 = 1, \tag{S10}$$

$$\frac{1}{N_u}\sum_{\sigma}\left(V\langle p^{\dagger}_{\sigma}f^{2}_{\sigma}\rangle + h.c.\right) - 2r_2 l_2 = 0\,, \tag{S11}$$

$$\frac{1}{N_u}\sum_{\sigma}\langle f^{2\dagger}_{\sigma}f^{2}_{\sigma}\rangle - r_2^2 = 1\,. \tag{S12}$$

The filling is still fixed to be one per site.

Symmetry analysis of the interacting Green's function

We briefly note on the symmetry analysis of the interacting Green's function[57]. This utilizes the eigenvectors and eigenfunctions of the single-particle Green's function of an interacting multi-band system. The symmetry analysis as applied on the eigenvectors proceeds in a similar way as for the Bloch functions of noninteracting bands. The degeneracies of the eigenvectors imply the degeneracies of the peaks in the energy dispersion of the corresponding spectral function. Further details can be found in Ref. 57.

Search for new materials to realize the proposed topological semimetal phases driven by strong correlations

The search for candidate materials started with the retrieval of Ce compounds crystallizing in the space group P4/nmm (SG 129) from the Inorganic Crystal Structure Database (ICSD). Multiple entries were unified. Only materials containing Ce atoms in the unique 2c Wyckoff position were taken into account. This yields 142 chemical compounds as specified in Fig. 4(a). In the second step, the following entries were removed: Insulators (oxides, oxohalogenides, oxosulfides), off-stoichiometric phases and solid solutions, obviously good metals (based on valence considerations) and superconductors and related phases. The remaining 39 pure stoichiometric phases were predominantly ternary cerium compounds of pnictogens, chalcogens, and the silicon group elements [Fig. S4(a)]. The further selection has to be done by literature search and inspection of the measured physical properties (where available), as illustrated in the next subsection. Two examples resulting from such a search are identified as strongly correlated paramagnetic semimetals, $CePt_2Si_2$ and $CeRh_2Ga_2$, and are proposed as materials for the correlation-driven topological semimetal phases advanced here. A similar procedure applies to the case of SG 31 with Ce atoms. The 4 materials of this case are shown in Fig. S4(b).

We note in passing that magnetic materials are also of interest, even though they are not the focus of the present work. For example, in the case of SG 129, CeSbTe is a well-known material that hosts f-electrons[37]. However, it exhibits an antiferromagnetic order at $T_N = 2.7$ K, which breaks time-reversal symmetry. Still, the amount of entropy that has been measured in such a temperature range suggests that the system will be strongly correlated if it is tuned to a paramagnetic state. Thus, tuning these systems into their paramagnetic ground state is suggested as a means of realizing the Kondo-driven topological semimetal we have advanced here.

$CeRh_2Ga_2$ and $CePt_2Si_2$ as strongly correlated semimetals

The two candidate materials we have identified, $CeRh_2Ga_2$ and $CePt_2Si_2$, show properties that are characteristic of strongly correlated semimetals. Their strong correlations are signaled by the large enhancement of the specific heat from the typical values of weakly correlated metals. The electronic specific-heat coefficient C/T reaches 130 and 80 mJ/mol K^2, respectively[47,48] (*i.e.* about 100 times the effective mass of weakly correlated bulk metals). Their semimetal nature is captured by the resistivity as a function of temperature, respectively shown in Fig. S5(a)(b) for the two compounds[47,59], which behaves similarly as Fig. S5(c)(d), respectively, for the well-established heavy-fermion semimetals $Ce_3Bi_4Pd_3$ and CeNiSn[20,49]. In all cases, the temperature dependence of the resistivity is neither activated, as a fully-gapped system would be, nor showing a giant T^2-dependent component at low temperatures with a positive temperature slope, as a typical heavy-fermion metal would be. This feature is accompanied by the relatively large magnitude of the resistivity.

Further details and additional results of the DFT calculations

The electronic structure calculations were performed using the Vienna ab initio simulation package (VASP)[60,61] with the Perdew, Burke and Ernz-erhof (PBE) generalized gradient approximation for the exchange correlation potential[62]. The f states were removed from the pseudo-potential to model the band structure. The interaction between the ion cores and valence electrons was described by the projector augmented-wave method[63]. The Hamiltonian contained the scalar relativistic corrections, and the SOC was taken into account by the second variation method[64].

The calculation for $CeRh_2Ga_2$ is in principle more difficult, given that the Rh- and Ga-site displacive disorder in the existing materials has been reported[65]. To get a qualitative understanding, we have carried out f-core DFT calculations but ignoring the disorder, with the Rh and Ga atoms fully assigned to the 2c and 2a sites, respectively. The results are shown in Fig. S7.

A realistic periodic Anderson lattice model can be constructed as follows. One can start from a

tight-binding representation for the conduction electrons based on the understanding of the dominant orbitals that form the spd conduction-electron bands; to illustrate the latter, we have analysed the atomic and orbital contents in the case of $CePt_2Si_2$, finding the dominating contributions to come from the Pt d- and s-orbitals (Fig. S8). One also needs to determine the lowest Kramers doublet for the f-electrons, which is an interacting problem; in practice, this usually requires input from spectroscopic measurements. Thereafter, one can construct the hybridization matrix.

Specific heat

To calculate the low-T specific heat, we focus on the linear-dispersion regime where we can approximate the dispersion $\epsilon_{\mathbf{k}} = \epsilon_{\mathbf{k}_\perp} = \hbar v^* k_\perp$. Here, $\mathbf{k} = (k_\parallel, \mathbf{k}_\perp)$ represents the decomposition of the wave vector into the components parallel and perpendicular to the nodal line; $\mathbf{k}_\perp$ itself has two components.

The specific heat becomes

$$\begin{aligned} c_v &= \frac{\partial}{\partial T}\int_{\infty}^{+\infty} \frac{d\epsilon}{(2\pi)^3}\epsilon\rho(\epsilon)f(\epsilon) \\ &= \frac{\partial}{\partial T}\int_{-\infty}^{+\infty} \frac{d\epsilon}{(2\pi)^3}\epsilon\frac{2K\pi\epsilon}{(\hbar v^*)^2}\frac{1}{e^{\epsilon/k_BT}+1} \\ &= \frac{K}{(2\pi)^3}\frac{\partial}{\partial T}\int_0^{2\pi} d\theta \int_0^{k_K} dk_\perp \frac{2\pi(\hbar v^*)^3 k_\perp^2}{(\hbar v)^2}\frac{1}{e^{\hbar v^* k_\perp/k_BT}+1} \\ &= \frac{K}{2\pi}\frac{9\zeta(3)}{2}k_B\left(\frac{k_BT}{\hbar v^*}\right)^2, \end{aligned} \tag{S13}$$

where K is the length of the nodal line and $\zeta(3) \approx 1.202$. So the specific heat per unit volume is

$$c_v = \Gamma\, T^2\,, \tag{S14}$$

$$\Gamma = \tfrac{K}{2\pi}\tfrac{9\zeta(3)}{2}\tfrac{(k_B)^3}{(\hbar v^*)^2}\,. \tag{S15}$$

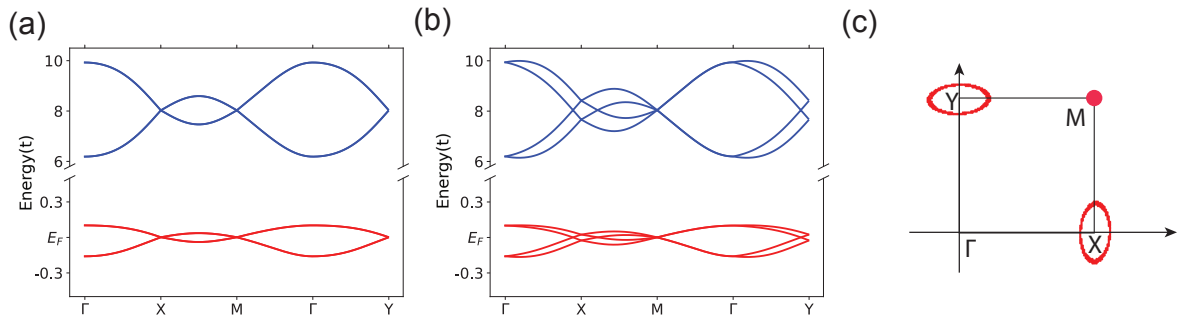


FIG. S1. **Kondo-driven composite fermions of a 2D square net. a,** The dispersion, including for the composite fermions (the lower red part), at $\Delta = 0$. The Kondo-driven Dirac nodes are pinned to E_F at the high-symmetry points X, Y, M. Here, the choice of parameters and the saddle-point analysis parallel those of Fig. 3(a). The input parameters are $(V, E_d, t_1, t_2, t^{SO}, \mu) = (6.8, -6, 1, 0, 0.6, -7.529)$. The saddle-point analysis yields $(r, l) = (0.285, -6.500)$. **b,** The dispersion of the Kondo-driven Weyl nodal-line semimetal. **c,** The Kondo-driven Weyl nodal lines (the red lines) encircle high symmetry points X and Y. Here $\Delta = 0.4$, and the other parameters are $(V, E_d, t_1, t_2, t^{SO}, \mu, r, l)$ = $(6.8, -6, 1, 0, 0.6, -7.564, 0.286, -6.500)$.

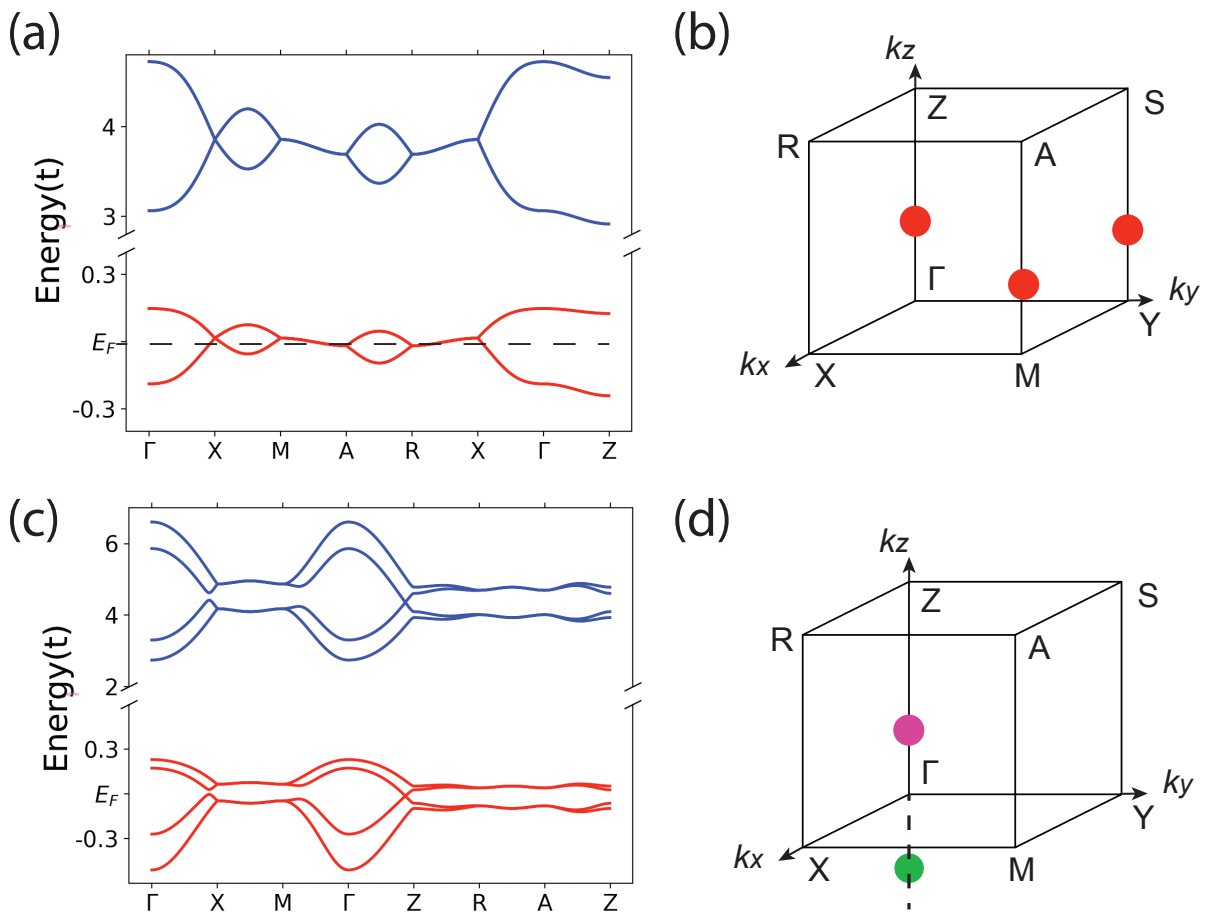


FIG. S2. **Kondo driven composite fermions in the 3D model for SG 129.** **a**, The dispersion, includes a symmetry enforced dispersive Dirac nodal line along $X - R$, $Y - S$ and $M - A$; and **b**, the points on the Dirac nodal line that cross the Fermi energy. The parameters for both **a** and **b** are $(t_1, t_2, t^{SO}, t_{1z}, t_{3z}, m_z, \Delta, V, E_d, \mu, r, l) = (1, 0, 0.4, 0.1, 0, 0, 0, 3.6, -2.6, -3.70, 0.44, -3.13)$; **c**, in the presence of a magnetic field, symmetry allows the existence of a pair of Weyl points along $\Gamma - Z$ as shown in **d**. The parameters are $(t_1, t_2, t^{SO}, t_{1z}, t_{3z}, m_z, \Delta, V, E_d, \mu, r, l) = (1, 0, 0.4, 0.1, 0.8, 0.3, 0, 3.6, -2.6, -3.82, 0.46, -3.53)$.

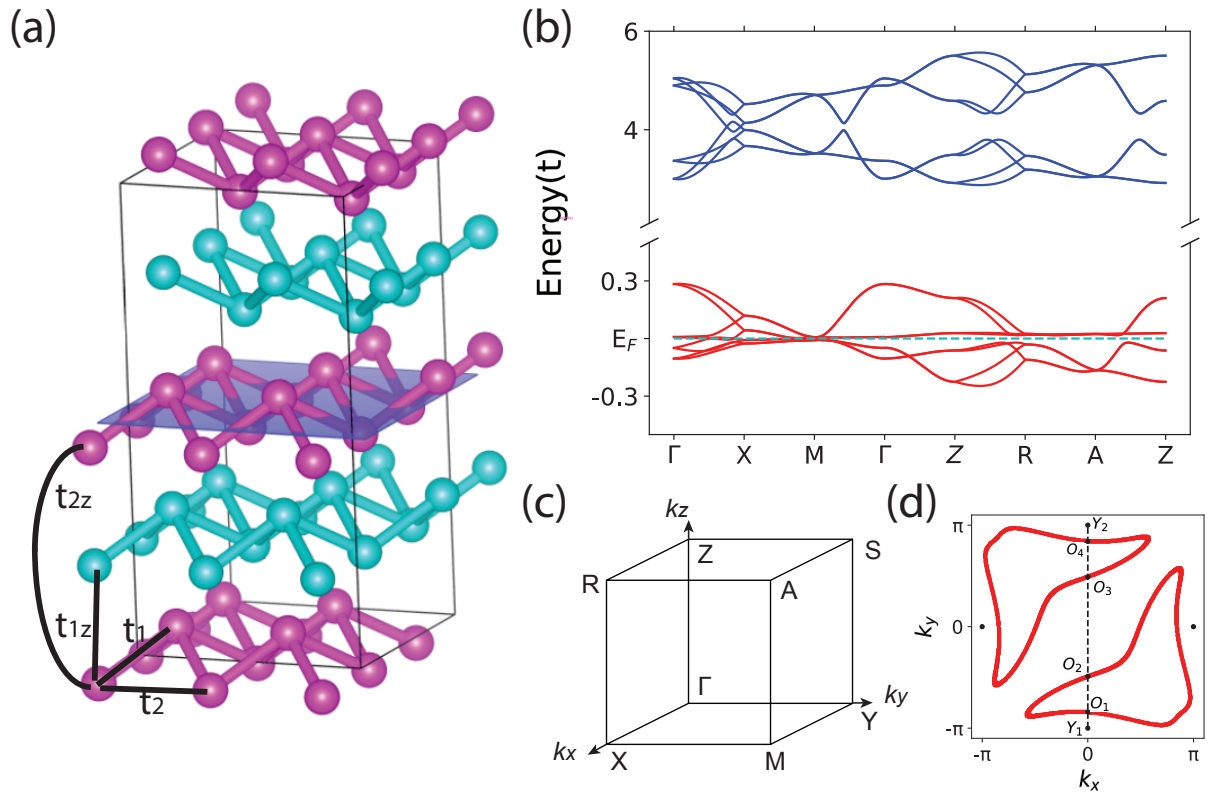


FIG. S3. **Kondo-driven composite fermions in the 3D model for SG 31 over an extended region of the Brillouin zone. a**, Illustration of the hopping parameters in the 3D-stacked model; **b,** The dispersion across both the $k_z = 0$ and $k_z = \pi$ planes with the same parameters as shown in Fig. 3. The composite fermions (lower red part) are fully gapped when $k_z \neq 0$. **c**, The 3D Brillouin zone with high symmetry points $\Gamma = (0, 0, 0)$, $X = (\pi, 0, 0)$, $Y = (0, \pi, 0)$, $M = (\pi, \pi, 0)$, $Z = (0, 0, \pi)$, $R = (\pi, 0, \pi)$, $S = (0, \pi, \pi)$ and $A = (\pi, \pi, \pi)$. **d,** The Kondo-driven Weyl nodal lines, which intersect with the dashed $k_x = 0$ line from $Y_1 = (0, -\pi, 0)$ to $Y_2 = (0, \pi, 0)$ at O_1, O_2, O_3 and O_4.

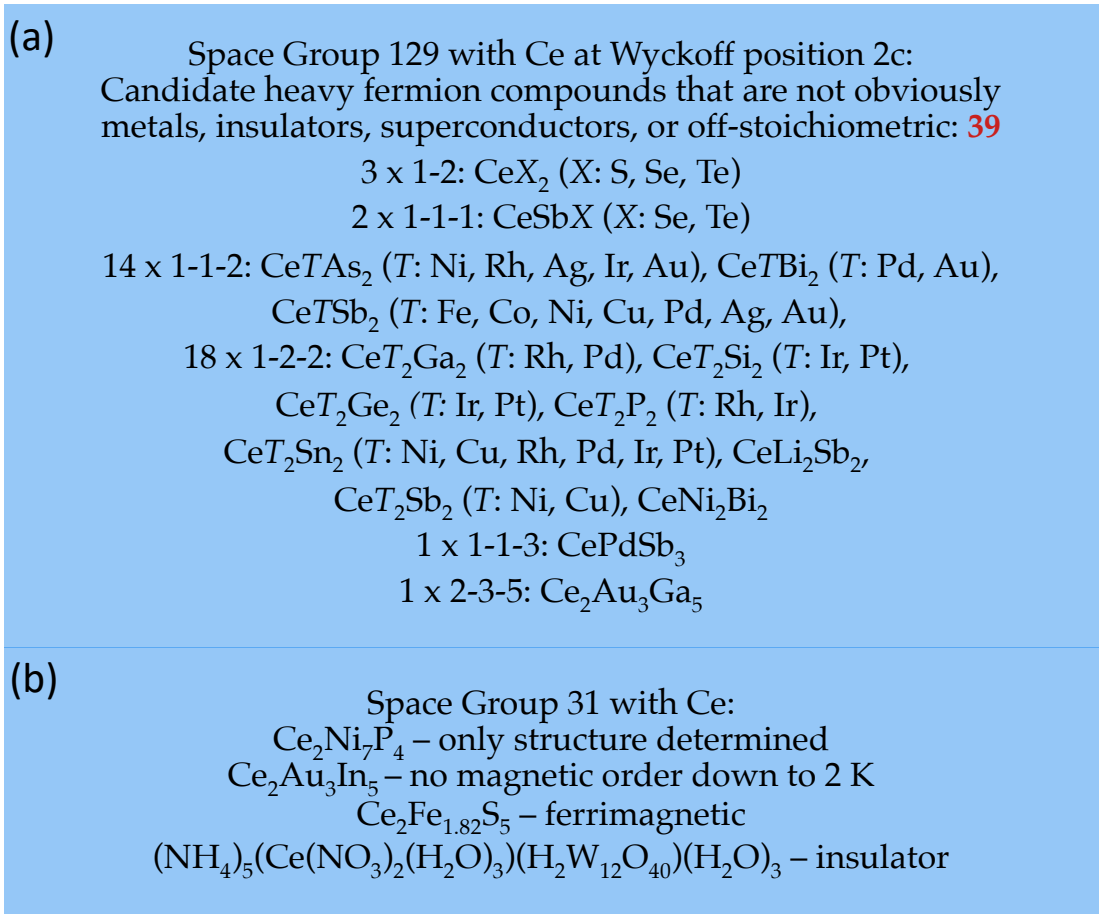


FIG. S4. **Further details in the search for correlation-driven topological semimetals.** Shown here are the materials identified during the intermediate step of the search procedure as outlined in Fig. 4(a) (main text) for SG 129 with Ce-ions on the Wyckoff position 2c (**a**) and in Fig. 4(b) (main text) for SG 31 with Ce atoms (**b**).

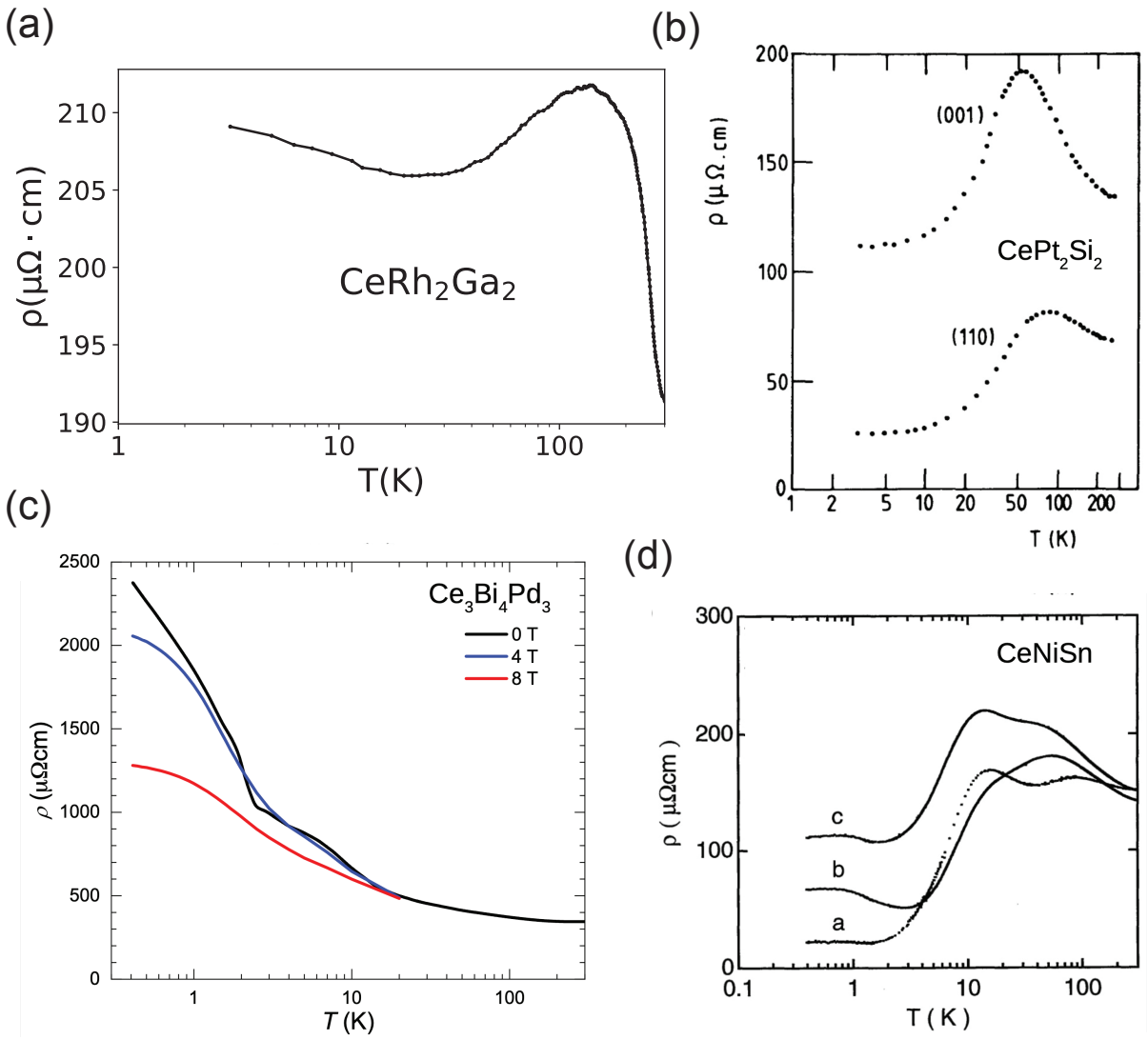


FIG. S5. **Semimetal transport of Ce-based square-net materials.** Resistivity (ρ) *vs.* temperature (T) of **a,** $CeRh_2Ga_2$ (replotted from Ref. 47), **b,** $CePt_2Si_2$[59], **c,** $Ce_3Bi_4Pd_3$[20], and **d,** $CeNiSn$[49]. All plots are shown in semi-log form.

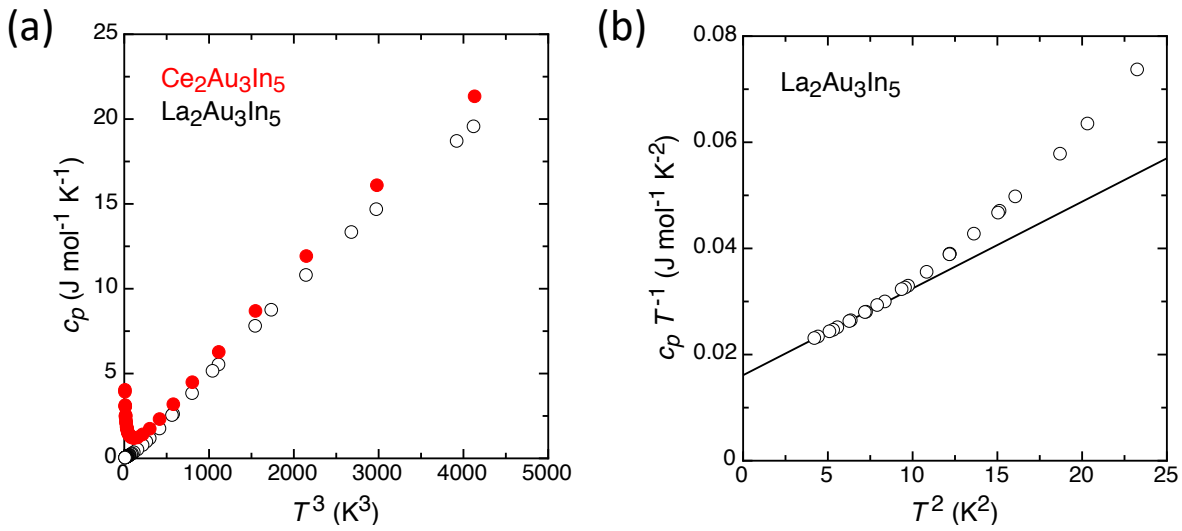


FIG. S6. **Specific heat of $Ce_2Au_3In_5$ and $La_2Au_3In_5$.** **a**, Total specific heat c_p as a function of T^3 for $Ce_2Au_3In_5$ (filled circles) and $La_2Au_3In_5$ (open circles). **b**, c_p/T of $La_2Au_3In_5$ as a function of T^2. The solid line is a Debye-Sommerfeld fit.

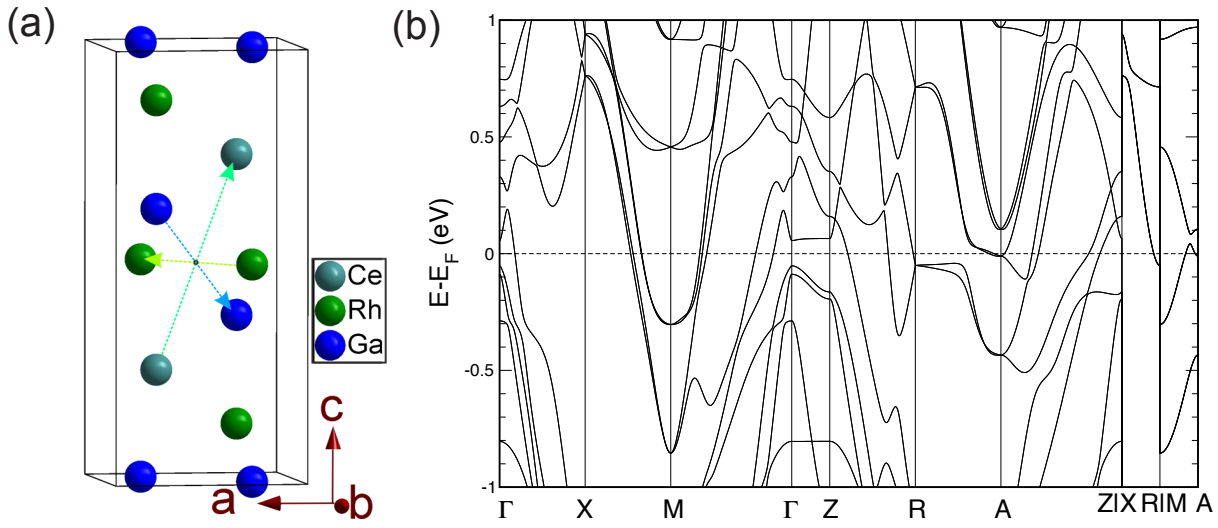


FIG. S7. **DFT results for** $CeRh_2Ga_2$**. a**, the crystal structure of $CeRh_2Ga_2$; **b**, the DFT results derived from ignoring the site-displacive disorder of the Rh and Ga atoms.

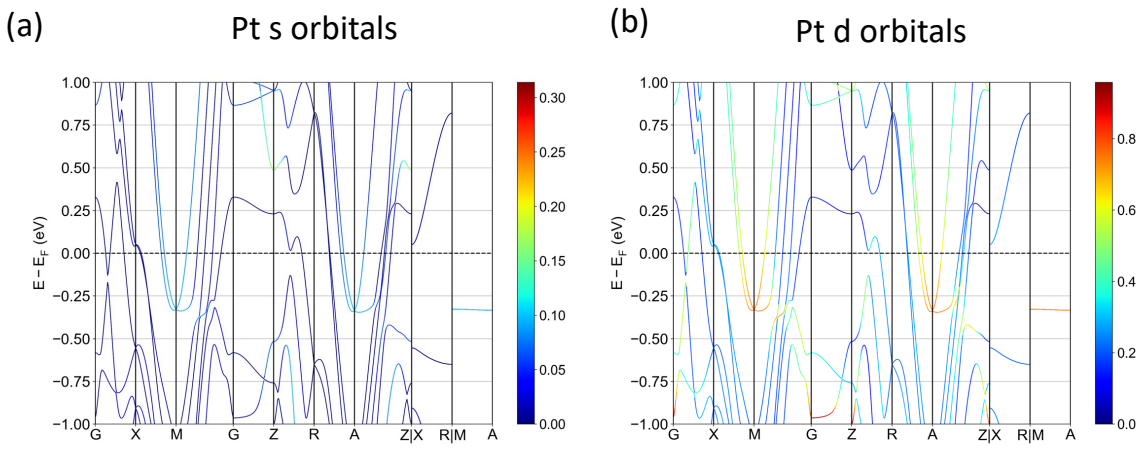


FIG. S8. **DFT results for the atomic and orbital contents of the** spd **conduction electrons in** $\mathbf{CePt_2Si_2}$**.** The dominating contributions are found to come from **a**, the Pt s-orbitals and **b**, the Pt d-orbitals. The bands have been plotted using PyProcar[66].